

JWST/NIRCam Coronagraphic Search for Hidden Planets in the HD 163296 Protoplanetary Disk

TAICHI UYAMA,^{1,2} LUCA RICCI,¹ MARIE YGOUF,³ SEAN ANDREWS,⁴ SARA GALLAGHER,¹ JANE HUANG,⁵ ANDREA ISELLA,^{6,7}
 DIMITRI MAWET,^{8,3} LAURA PÉREZ,⁹ MASSIMO ROBERTO,^{10,11} GARRETH RUANE,³ SHANGJIA ZHANG,^{5,12,13,*} AND
 ZHAOHUAN ZHU^{12,13}

¹*Department of Physics and Astronomy, California State University Northridge, 18111 Nordhoff Street, Northridge, CA 91330, USA*

²*Astrobiology Center, 2-21-1 Osawa, Mitaka, Tokyo 181-8588, Japan*

³*Jet Propulsion Laboratory, California Institute of Technology, 4800 Oak Grove Dr., Pasadena, CA, 91109, USA*

⁴*Center for Astrophysics, Harvard & Smithsonian, 60 Garden St., Cambridge, MA 02138, USA*

⁵*Department of Astronomy, Columbia University, 538 W. 120th Street, Pupin Hall, New York, NY 10027, USA*

⁶*Department of Physics and Astronomy, Rice University, 6100 Main St, Houston, TX 77005, USA*

⁷*Rice Space Institute, Rice University, 6100 Main St, Houston, TX 77005, USA*

⁸*Department of Astronomy, California Institute of Technology, 1200 E. California Blvd., Pasadena, CA 91125, USA*

⁹*Departamento de Astronomía, Universidad de Chile, Camino El Observatorio 1515, Las Condes, Santiago, Chile*

¹⁰*Space Telescope Science Institute, 3700 San Martin Drive, Baltimore, MD 21218, USA*

¹¹*Department of Physics & Astronomy, Johns Hopkins University, 3400 N. Charles Street, Baltimore, MD 21218, USA*

¹²*Department of Physics and Astronomy, University of Nevada, Las Vegas, 4505 S. Maryland Pkwy, Las Vegas, NV, 89154, USA*

¹³*Nevada Center for Astrophysics, University of Nevada, Las Vegas, Las Vegas, NV 89154, USA*

Submitted to AAS Journals

ABSTRACT

HD 163296 is a Herbig Ae/Be star with multiple signposts of on-going planet formation on its disk, such as prominent rings and gaps, as well as kinematic features as identified by previous ALMA observations. We carried out JWST/NIRCam coronagraphic imaging using the F410M and F200W NIRCam filters, with the goal of detecting the emission from the putative young planets in this system. Our F410M observations did not detect the putative planets at the predicted locations of the ALMA velocity kinks, but detected a point-like source candidate at a separation of $\approx 0''.75$ and a position angle of $\approx 231^\circ.4$ that is unlikely a background star because of the measured flux in the F410M filter and the detection limit in the F200W filter. These data achieved unprecedented contrast levels at $\sim 4 \mu\text{m}$ at stellocentric separations $\rho \gtrsim 0''.8$. This allowed us to derive stringent constraints at the outer velocity kink ($\Delta F410M = 15.2$ mag) on the mass of the putative planet with or without a circumplanetary disk, and considering different possible initial entropies for the planet.

Keywords: Exoplanets, Planet Formation, Protoplanetary Disks, James Webb Space Telescope, Coronagraphic Imaging

1. INTRODUCTION

The discovery of thousands of exoplanets over the last couple of decades has shown that the birth of planets is a very efficient process in nature (e.g., Burke et al. 2015). However, several of the physical mechanisms responsible for their formation and evolution are still poorly understood. Starting with the very first detection of an exoplanet around a

Solar-like star (Mayor & Queloz 1995), the discovery of hot Jupiters very close to their star has suggested that the orbits of planets can significantly vary during their life (Lin et al. 1996). A natural explanation for this migration of planets involves the gravitational interaction between the still-forming planet and the parental disk (see, e.g., the review by Baruteau et al. 2014). The theory of planet-disk interaction predicts that planets interact with the disk by launching density waves, and the consequent torque on the planet can lead to planet migration.

* NASA Hubble Fellowship Program Sagan Fellow

Although theoretical investigations of the disk-planet interaction have been conducted for several decades (Lin & Papaloizou 1979; Goldreich & Tremaine 1979), this theory still needs empirical validation. Observations at optical and near infrared wavelengths predominantly trace stellar radiation scattered by fine dust grains on the upper layers of the disk, and may not directly reflect the spatial distribution of solids in the planet-forming disk regions. The distribution of solids in the dense disk regions can be investigated at longer sub-mm/mm wavelengths, for example with ALMA, because of the lower optical depths of the dust emission.

Altogether, these observations of nearby protoplanetary disks have unveiled annular gaps, cavities, and spiral arms in the disk that may be produced by the interaction with planets (for recent reviews, see Bae et al. 2023; Paardekooper et al. 2023). The most common disk substructures are concentric gaps and rings observed in the sub-mm continuum with ALMA (e.g., Andrews et al. 2018; Huang et al. 2018). In several cases the morphology of these structures are consistent with the predictions of models of planet-disk interaction, and their observational properties have been used to estimate the mass of the putative planets (e.g., Kanagawa et al. 2015; Dipierro et al. 2018; Zhang et al. 2018; Lodato et al. 2019).

Although concentric rings and gaps, as well as most of the other observed structures, are compatible with the hypothesis of one or more embedded planets in those systems, they are not unique to that scenario. In fact, several processes, such as molecular condensation fronts (Banzatti et al. 2015), photoevaporation (Owen et al. 2010), and also various magneto-hydrodynamical instabilities have been shown to produce comparable structures in the disk - e.g., magneto-rotational instability (Flock et al. 2015); zonal flows (Uribe et al. 2011); radially variable magnetic disk winds (Suriano et al. 2018), and vertical shear instability (Flock et al. 2015). Given the multi-dimensional parameter space of the models, the best way to discriminate between scenarios of disk-planet interaction vs disk chemical/physical mechanisms is to detect planets.

A particularly interesting disk where to study planet formation and planet-disk interaction is the HD 163296 system. HD 163296 is a young intermediate mass ($M_\star \approx 2 M_\odot$, Andrews et al. 2018) Herbig Ae star located at 100.97 ± 0.42 pc from Earth (Gaia Collaboration et al. 2016, 2023). The star is surrounded by a gaseous disk with a radius of about 500 au. In contrast, mm-wave continuum emission arising from solid particles is confined within about 200 au from the star (Isella et al. 2007; de Gregorio-Monsalvo et al. 2013). Isella et al. (2018) and Huang et al. (2018) imaged this disk using ALMA in the dust continuum at 1.3 mm with an angular resolution of about $0''.04$, or 4 au at the distance of the source. These observations unveiled four annular concentric gaps (or dark annuli) centered at about $0''.10$, $0''.48$, $0''.86$, and $1''.45$ from

the star, corresponding to stellocentric radii of 10 (gap D10), 48 (D48), 86 (D86), and 145 au (D145), respectively. The analysis of the radial profile of the continuum surface brightness shows that the bright rings are radially narrow, and interleaved by wide gaps. For example, the inferred radial widths of the D48 and D86 gaps are of about 20 – 30 au, and for the D145 gap of about 40 – 50 au, respectively (Isella et al. 2016, 2018). These are among the widest gaps detected within the disks imaged at high-resolution with ALMA by the Disk Substructures at High Angular Resolution Project (DSHARP; Andrews et al. 2018).

The outer gaps D86 and D145 show depletion also in CO gas density (Isella et al. 2016). The widths and levels of mass depletion inferred for the dust and gas density of the HD 163296 disk favor the hypothesis of young giant planets opening those gaps, and are less consistent with alternative scenarios involving chemical processes such as molecular condensation fronts. Furthermore, the high mass accretion rate $\dot{M} \approx 5 \times 10^{-7} M_\odot \text{ yr}^{-1}$ derived for HD 163296 (Mendigutía et al. 2013) is less compatible also with disk photoevaporation from high-energy stellar photons to form any of these gaps. Liu et al. (2018) used the LA-COMPASS hydrodynamic code (Li et al. 2005, 2009) to reproduce the multi-ring structure seen in HD 163296. This code accounts for the gravitational torques induced by planets in the disk, as well as the aerodynamic interaction between gas and dust. The D86 and D145 gaps are consistent with being opened by young giant planets with masses close to the one of Jupiter. Similar results were obtained, and extended to the inner gaps D10 and D48, by Zhang et al. (2018).

Moreover, ALMA observations of the CO molecular line emission have detected significant deviations from the expected emission for a disk in Keplerian rotation, which are consistent with perturbations induced by the gravitational interaction with Jupiter-mass planets in the D86 and D145 outer gaps (Teague et al. 2018; Izquierdo et al. 2022, 2023). Teague et al. (2019) analyzed the 3D kinematical structure of the disk and found evidence for meridional (vertical) flows of gas that they reproduced using disk models containing planets with masses of $\approx 1 - 2 M_{\text{Jup}}$ in the D86 and D145 gaps, as well as at an outer orbit of 237 au from the central star. More localized perturbations in the kinematics of the Keplerian disk, known as ‘velocity kinks’, have been reported by Pinte et al. (2018, 2020) in the ALMA channel maps for the ^{12}CO ($J = 2 - 1$) emission line at angular separations from the star and position angles (East of North) of ($2''.20$, -3°) for kink #1 and ($0''.67$, 93°) for #2, respectively. These locations are consistent with the D86 gap and with the stellocentric radius of the outer meridional flow (Teague et al. 2019). Also these localized kinematical features are reproduced by models of disk-planet interaction with planets with a mass of $\approx 2 M_{\text{Jup}}$.

Young disks with wide and cleared annular gaps are therefore excellent targets to attempt the direct detection of young planets and to test the predictions of planet-disk interaction models. However, detecting newborn planets is challenging: the variability of young stars and the presence of dusty disks hinder the use of radial velocities and transit techniques. Direct imaging techniques at optical-infrared wavelengths have the potential to detect young planets that are distant from the star (> 5 au) and that have cleared the tenuous external disk regions to expose themselves, though the number of detections is small (see a review by Currie et al. 2023). With the exception of the convincing embedded planets in the PDS 70 system (Keppler et al. 2018; Haffert et al. 2019) and some other planet candidates (e.g., AB Aur b, MWC 758c, and HD 169142b; Currie et al. 2022; Wagner et al. 2023; Hammond et al. 2023), other high-contrast imaging surveys did not detect planets embedded in disks (e.g., Uyama et al. 2017; Cugno et al. 2019; Asensio-Torres et al. 2021; Cugno et al. 2023; Wallack et al. 2024). Several high-contrast imaging observations searched for embedded planets also in the HD 163296 system (e.g., Guidi et al. 2018; Mesa et al. 2019; Rich et al. 2019; Xie et al. 2020; Hasegawa et al. 2024), but did not detect any convincing planet signal. We carried out new coronagraphic observations of the HD 163296 system using the *Near Infrared Camera* (NIRCam) aboard the *James Webb Space Telescope* (JWST). The main goal of these observations is to investigate the presence of the planets that have been proposed to explain the disk structures observed in this system.

In this paper, we present the results of the new JWST/NIRCam observations of the HD 163296 system. Section 2 presents the main characteristics of these observations together with the methods adopted for the data reduction; the results of these observations are outlined in Section 3 and discussed in Section 4. Section 5 summarizes the main findings of this work.

2. OBSERVATIONS AND DATA REDUCTION

2.1. NIRCam Observations

We observed HD 163296 with JWST/NIRCam (Rieke et al. 2005) under the Cycle 1 GO 2540 program (PI: Luca Ricci)¹.

Primary observations of the HD 163296 system utilized the Lyot round masks in two filters, i.e. MASK210R for F200W in the SHORT channel (SUB640A210R subarray, pixel scale $\approx 0''.031/\text{pix}$), and MASK430R for F410M in the LONG channel (SUB320A430R subarray, pixel scale $\approx 0''.063/\text{pix}$), respectively. NIR-

Cam enables simultaneous exposures at the SHORT and LONG channels while one Lyot mask is used. In total, we obtained four-configuration observations: primary F200W/MASK210R and F410M/MASK430R, and by-product F200W/MASK430R and F410M/MASK210R. Our program did not observe a PSF reference star for reference-star differential imaging (RDI) because HD 163296 is known to have a strong infrared excess emission due to circumstellar dust very close to the star, but employed roll-subtraction angular differential imaging (ADI) by obtaining the data at two roll positions for post-processing to remove the stellar PSF. The readout pattern was set to 'MEDIUM8', and the total exposure times were 9220.69 seconds per roll (19841.38 seconds in total) for the F410M/MASK430R and F200W/MASK430R observations, and 8057.75 seconds per roll (16115.48 seconds in total) for the F200W/MASK210R and F410M/MASK210R observations. The roll angle difference for ADI was $10^\circ 35'$.

The secondary by-product configurations, i.e. F200W/MASK430R and F410M/MASK210R, however, were not as useful as the primary ones for the detection of embedded planets: in the F200W/MASK430R image the central star is located close to the edge of the field of view (FOV), and the F410M/MASK210R image suffers from intense starlight residuals within a few arcseconds from the central star, leaving significantly more residual speckles and producing worse contrast levels than in the primary data with MASK430R (see Appendix A). Hereafter, 'F200W' and 'F410M' refer to the primary configurations of F200W/MASK210R and F410M/MASK430R, respectively.

2.2. NIRCam Data Reduction

2.2.1. Pre-processing

We downloaded the stage 0 datasets (*uncal.fits), and then used the spaceKLIP pipeline² (version 2.1.1; Kammerer et al. 2022; Carter et al. 2023) for data calibration (with the JWST pipeline; Bushouse et al. 2023, for stage 0 to 2), which is customized for coronagraphic imaging (see Carter et al. 2023). The version of JWST calibration reference data system (CRDS) file we used is 11.17.14.

Particularly before the post-processing steps to search for faint sources around HD 163296 by PSF subtraction (stage 2 to 3), we read the stage 2 datasets (*calints.fits) into the spaceKLIP Database class and then operated pre-processing functions in the imageTools class to conduct background subtraction, bad-pixel correction (masking and interpolation), image centering (from the mask center to the PSF centroid) and alignment (correcting frame-to-frame shifts). To further mitigate the effect of potential speckles that are not static during the observations, we applied pixel-

wise sigma-clipping (3σ) for the integrations in each FITS file after the image alignment process. We also excluded outlier integration frames that deviate by $> 3\sigma$ from the averaged integration image and those with noisy speckles, which we identified by visually checking all integration frames. In total we removed one integration frame (corresponding to an exposure time of about 62 seconds) from the F410M data set and nine frames (exposure time of about 263.7 seconds) from the F200W data set.

2.2.2. Post-processing

After pre-processing, we aimed at subtracting stellar halo leaking the coronagraph mask and instrumental speckles that hinder faint planet signals from the science exposures by producing the best representation of the PSF. We made use of the `pyKLIP` modules in the `imageTools` class, which is a statistical post-processing pipeline used for differential imaging data through the Karhunen-Loève Image Processing algorithm (KLIP; Soummer et al. 2012). Regarding the `pyKLIP` parameters, we did not divide the FoV into several subsections with the ‘annuli’ and ‘subsections’ parameters because there are numerous objects (e.g., background objects and the disk features, see Section 3) in the FoV, and dividing the FoV into several subsections could induce artifacts, particularly in the presence of bright nearby sources. Instead, we cropped the FoV into a $10'' \times 10''$ area before running `pyKLIP` modules. As previous studies predicted embedded protoplanets in the HD 163296 disk at stellocentric separations $\rho \lesssim 2''.5$, this paper focuses on sources within $2''.5$ from the central star, while outer sources will be discussed in a future work. As the field rotation for ADI is ≈ 10 deg, the most aggressive PSF subtraction can attenuate faint or extended features; in order to mitigate this effect, we adopted small values for KL modes for moderately aggressive ADI reduction when showing our post-processed images in Section 3, although we also show the post-processing results which can be obtained with other values for the KL modes in Appendix B.

As mentioned in Section 2.2.1 we did not observe a PSF reference star. Moreover, at the moment there are no archival data for reference stars observed in the same configurations as our program. We attempted to employ RDI by generating synthesized reference PSFs using `WebbPSF` (Perrin et al. 2014), and incorporating wavefront errors taken on the closest date to our observations. However, we did not achieve as high-contrast performance as with the ADI reduction (see Appendix C for the results of this attempt using RDI).

3. RESULTS

3.1. Post-processed results

The post-processed JWST/NIRCam images are shown in Figure 1. We detected numerous sources in both filters but in this study we focus on the $6''$ by $6''$ region around the cen-

tral star (bottom panels in Fig. 1) where we expect planets in the HD 163296 disk. Especially in our F200W map, a difference is evident in the number density of background sources between the regions within and beyond the HD 163296 outermost ring feature (at separations $\rho \sim 2''.5 - 3''.5$, see below); this is a clear signature of the extinction of light from background sources due to dust in the disk (see also theoretical predictions in Sanchis et al. 2020; Marleau et al. 2022; Hasegawa et al. 2024; Alarcón et al. 2024). We note that the elongated features visible towards the South-West corner in the F200W map is a cluster of bright background sources with diffraction patterns from the NIRCam PSF and self-subtraction features caused by the ADI reduction (cf. SPHERE HD 163296 data; Mesa et al. 2019; Juillard et al. 2024).

Our NIRCam observations did not detect significant IR emission from the putative protoplanets at the locations of the velocity kinks observed with ALMA, but at the same time some interesting features are visible on the images: 1) a compact source with a contrast of 1.8×10^{-5} at $\rho \approx 0''.75$ and a position angle of $\approx 231^\circ.4$ in the F410M image, which does not have a counterpart in the F200W image (see Figure 2); 2) two arc-like features were clearly detected, such as R1 ($\rho \sim 0''.45$ to the North of the star) in the F410M image and R3 ($\rho \sim 2''.2$ to the North) in the F200W image (see Figure 2), while two other similar features are less clear, such as R0 (very close to the star) and R2 ($\rho \sim 0''.7$ to the North); in the rest of the paper we refer to these features as *rings* because these arc-like features are likely the forward-scattering side of more extended ring structures, as shown by previous studies (e.g., Guidi et al. 2018; Mesa et al. 2019; Rich et al. 2019; Juillard et al. 2024); 3) the resolved ring feature in the F200W image (R3) is in close proximity with the outer velocity kink (see the right panel in Figure 2). Detailed discussions of these features are provided in the following subsections.

3.2. Search for Embedded Protoplanets

We searched for point-like sources on the post-processed F410M image within the disk region. In order to consider a point-like feature as a source candidate we requested that 1) the point-like source is surrounded by adjacent self-subtraction features caused by ADI reduction, and that 2) its signal does not significantly vary at different KL modes. Note that large KL modes lead to aggressive PSF subtraction causing heavy self-subtraction, leading to attenuation of any signal particularly at small separations (see also Appendix B), and we prioritized small KL modes. We then attempted forward modeling and PSF fitting using the `extract_companions` module (cf, `pyklip.fitspsf`; Wang et al. 2015) for quantitative investigations. We found one point-like feature (indicated by a circle in Figure 2) is well fitted with the forward-modeled PSF. Table 1 summa-

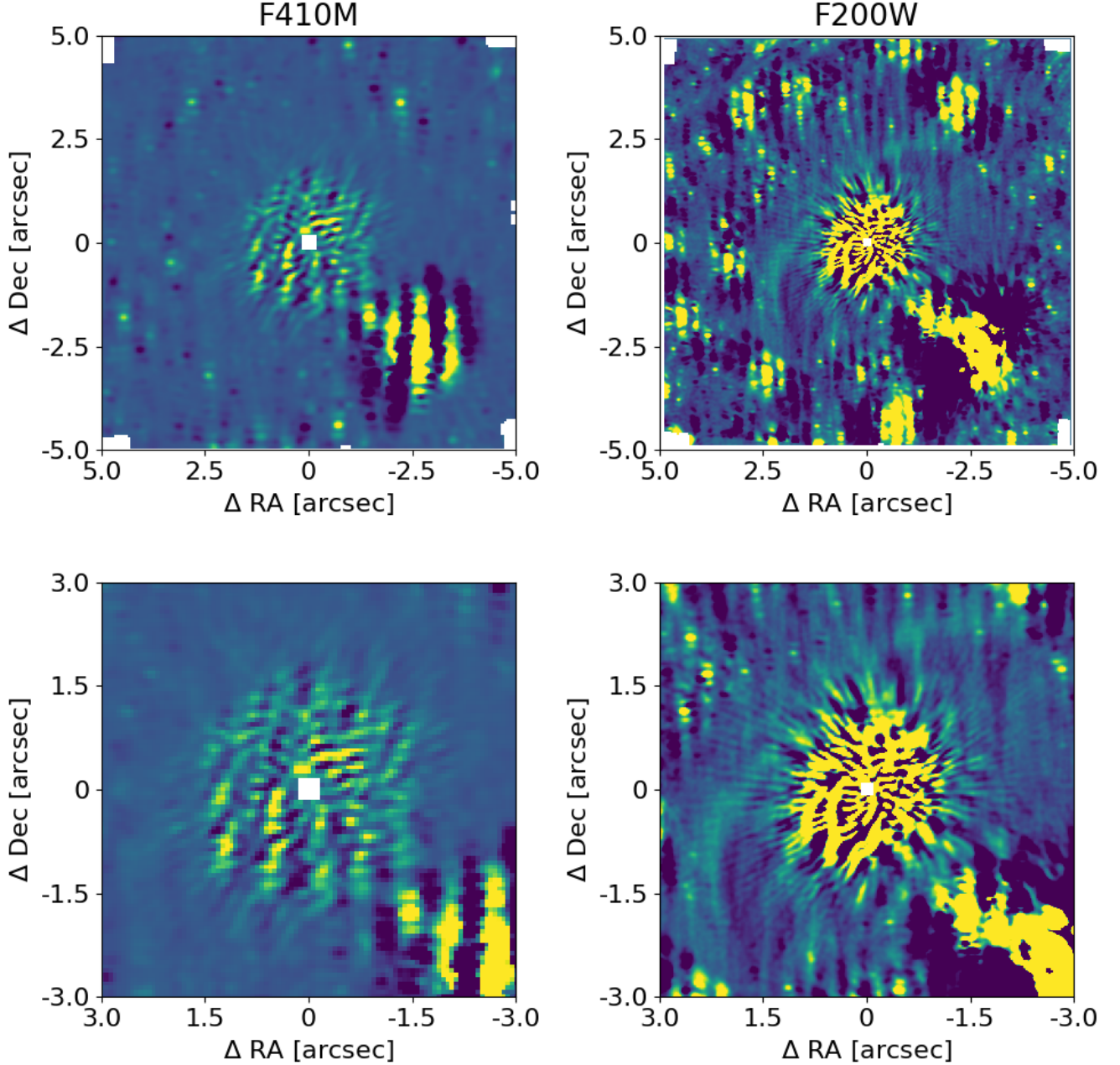


Figure 1. Top: Post-processed JWST/NIRCam maps in the F410M (left) and F200W (right) filters, obtained with KL=3. Bottom: Zoomed-in images of the post-processed results (top).

izes the photometry and relative astrometry and Figure 3 shows the PSF fitting result at different KL modes. The noise here was measured as the standard deviation on the residual map within a local $\sim 1'' \times 1''$ box around the source candidate (the upper right panel in Figure 3). Typically the noise in high-contrast imaging is measured as the standard deviation within annular regions assuming the noise to be azimuthally symmetric. However, our data show the disk

feature that can contribute to noise and azimuthally asymmetric speckle residuals due to the small field-rotation ADI processing and the PSF of NIRCam coronagraphic imaging. We note that the SNR and the extracted contrast decrease at $KL \geq 5$ because of a significant self-subtraction effect via aggressive ADI subtraction at such a small separation from the star, making the extracted photometry and SNRs at such large KLs unreliable (cf, Appendix B). In contrast at small

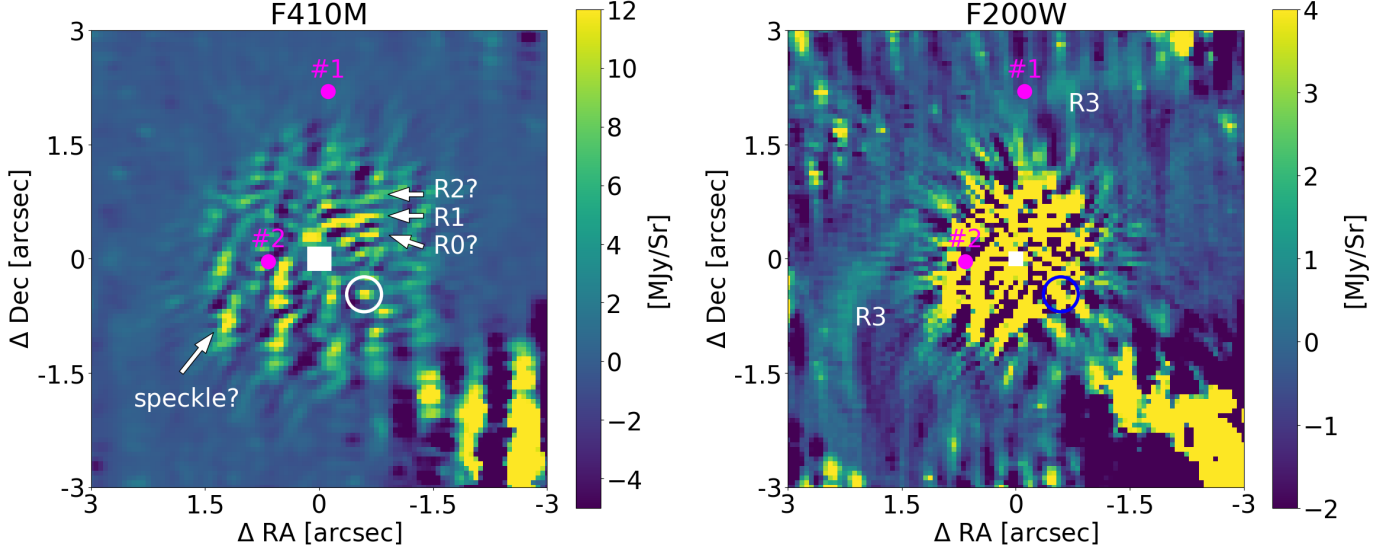


Figure 2. NIRC2 F410M (left) and F200W (right) maps as in the bottom panels in Figure 1 with symbols representing the predicted locations of putative protoplanets from the velocity kinks observed with ALMA (indicated by magenta dots with the kink ids; Pinte et al. 2020), a point-like source candidate (white and blue circles in the left and right panels, respectively), and ring features (R0–R3).

Table 1. Information on the source candidate from the F410 NIRC2 map (KL = 1).

Stellocentric Separation	Position Angle	Contrast	SNR
$0''.754 \pm 0''.007$	$231^\circ.39 \pm 1^\circ.27$	1.83×10^{-5}	5.0

KLs (KL = 1–4) the extracted contrast level is more stable. There are several other relatively bright features at marginal SNRs, but they are spatially extended, suggesting that they are likely residual speckles (e.g. the annotated extended feature (‘speckle?’) in the left panel of Figure 2).

PSF fitting of the compact source at KL=1 provides a contrast estimate of 1.8×10^{-5} , corresponding to an apparent magnitude in F410M of 15.03 ± 0.15 . Regarding the flux of the central star, which was used to convert the contrast estimate into an apparent magnitude, we collected available photometric information from VO Sed Analyzer (VOSA; Bayo et al. 2008) and read it into spaceKLIP, which derived the corresponding stellar magnitude at each filter, i.e. 4.97 ± 0.02 mag at F200W, and 3.20 ± 0.07 mag at F410M. Given the relatively marginal SNR of this source, future observations will be needed to confirm this detection. In Section 4.1, we discuss the plausibility of different scenarios for the nature of this source given the information at our disposal.

3.3. Disk Features

Our NIRC2 observations in the F410M filter resolved the ring feature R1, which was reported by previous ground-based high-contrast imaging observations (e.g., Guidi et al. 2018; Mesa et al. 2019; Rich et al. 2019; Juillard et al. 2024). Although the R1 ring is also marginally seen in the

F200W post-processed image, regions at such inner separations ($\rho \lesssim 1''$) are speckle-dominant. Other ground-based high-contrast observations have achieved higher contrast levels within $1''$ from the star at NIR wavelengths and detected the R1 feature more clearly (e.g., Mesa et al. 2019; Rich et al. 2019).

The F410M map shows potential additional ring-like features other than R1 (see the left panel of Figure 4 and Appendix B for different KL modes). However, the regions in the map with separations from the star $\rho \lesssim 1''.5$ are affected by residual speckles and the bright disk feature R1 might induce other diffraction patterns, which can mimic arc-like features. Tentative evidence for R2 was found in an archival Keck/NIRC2 M_s -band dataset that marginally detected another arc-like feature just outside of R1 (see Appendix E). R2 is seemingly collocated with an extended feature right outside of R1 in the F410M post-processed image (denoted as ‘R2?’ in Figure 2). The presence of R2 suggests that the companion candidate reported in Guidi et al. (2018) may be part of R2.

To test whether these arc-like features in the F410M data are systematic diffraction patterns induced by R1 or real features (R1+R2), we forward-modeled a toy disk model with properties that resemble the R1 ring. As detailed in Appendix D, we found that this ring did not induce additional significant extended features.

We note that R2 has been detected only at $\lambda \gtrsim 3 \mu\text{m}$ with Keck/NIRC2 and JWST/NIRC2 while our F200W data as well as with previous high-contrast imaging at NIR wavelengths do not show evidence of R2 (e.g., Rich et al. 2019; Juillard et al. 2024). As mentioned in Guidi et al. (2018), R1 is not co-located with any of the ALMA bright rings, most

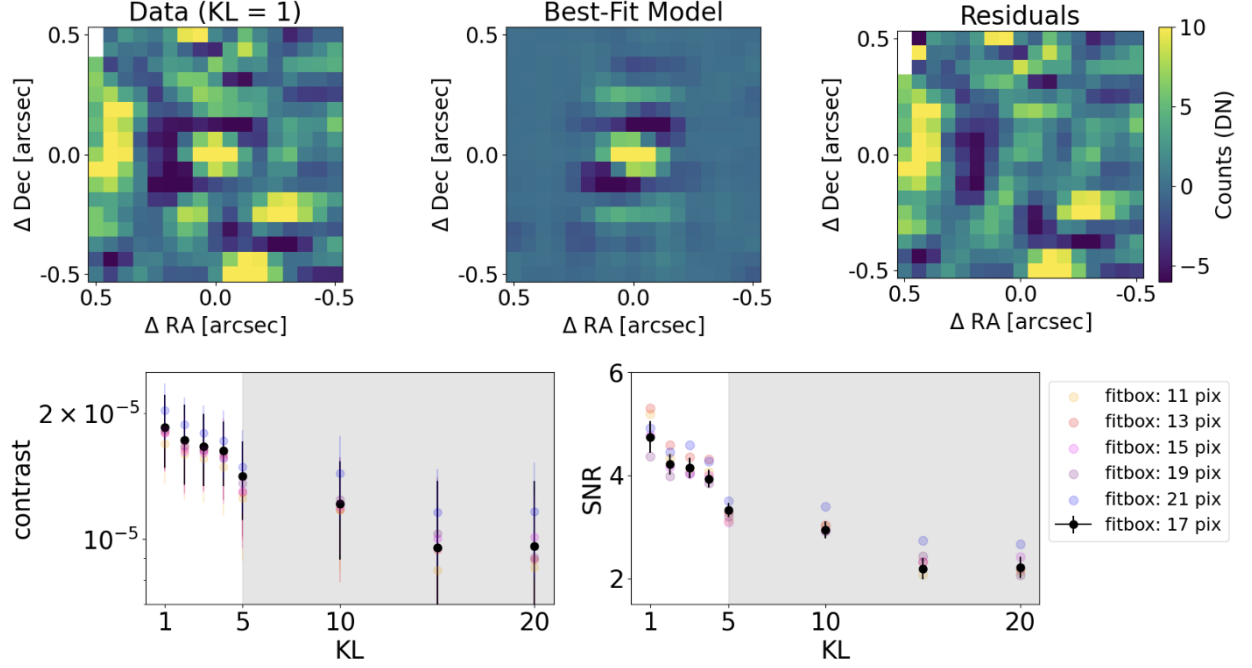


Figure 3. PSF fitting results of the source candidate with $KL=1$ (top panels), and the derived contrast and SNR values for different KL modes (bottom panels). The colors in the plot indicate the box size used for the PSF fitting, demonstrating that the extracted photometry and SNR do not largely depend on the size parameter. We finally adopted the 17-pix box corresponding to $\sim 1'' \times 1''$ (see text). The error bars of the 17-pix plot in the right panel correspond to the standard deviations of the SNR measurements among the 13–21 pixel range. The gray-shaded parameter space ($KL \geq 5$) indicates aggressive PSF subtraction and a heavy self-subtraction effect onto astronomical sources at $\sim 0''.75$, where the source candidate is located. See also Appendix B for the PSF fitting results at different KL modes.

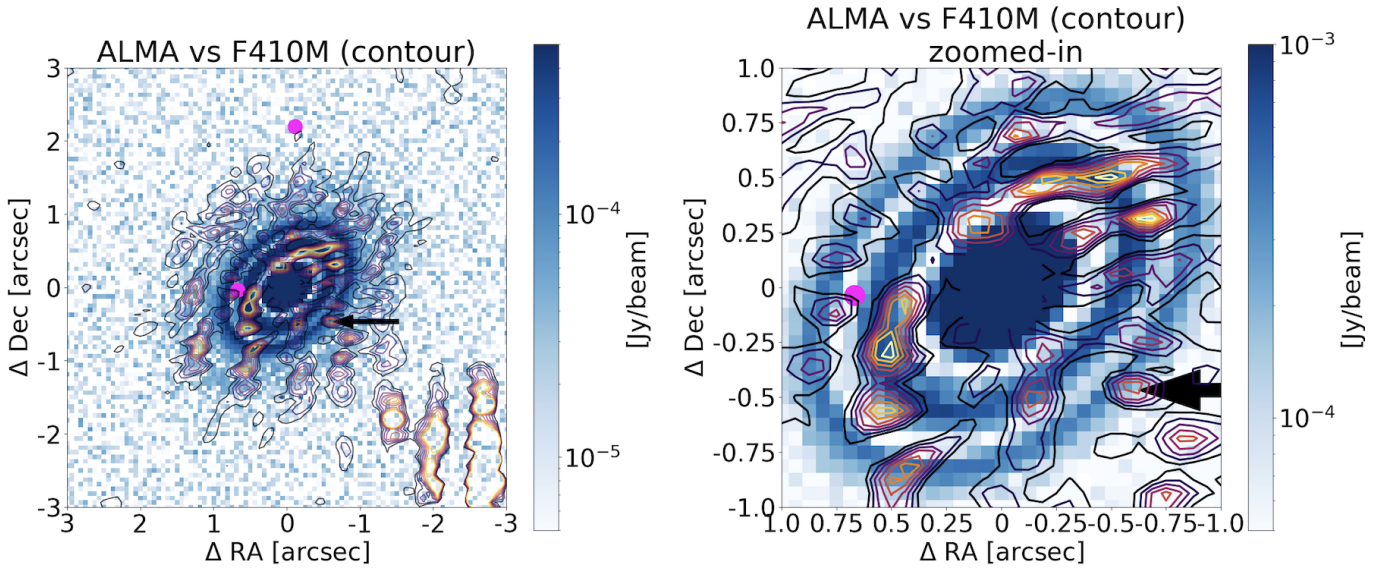


Figure 4. Comparison between the F410M map (contours) and the DSHARP ALMA continuum map (colors) at $\lambda = 1.3$ mm ($6'' \times 6''$ map in the left and $2'' \times 2''$ map in the right, respectively; Isella et al. 2018). The location of the source candidate is indicated by a black arrow. The magenta dots show the location of the ALMA velocity kinks.

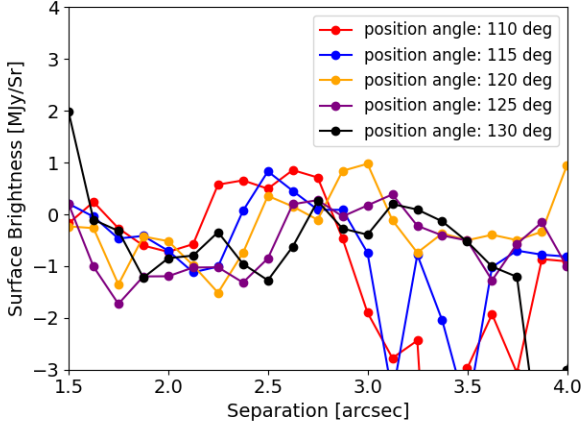


Figure 5. Radial profiles of the surface brightness at different position angles in the F200W image. The bump feature between $\sim 2'' - 3''$ at each position angle indicates the location of R3. The outer regions beyond R3 contain signal from background stars as well as negative self-subtraction features, making the radial profiles noisier than in the region inside of R3.

likely because scattered-light and dust thermal emission originate from different areas in a disk structure (cf., Ginski et al. 2016; Dong et al. 2018; Boehler et al. 2018). On the semi-minor axis direction (at a position angle of $\approx 43^\circ$; Huang et al. 2018), R1 has an offset of $\sim 0''.2$ from the spine of B67 and the whole feature overlaps with the ALMA rings/gaps (D45, B67, and D86; see the right panel in Figure 4), suggesting that R1 is generated by scattering of the light from the central star by a flared inner wall of B67 (cf., B67 is known to have a significantly large scale height; Doi & Kataoka 2021). Similarly, R2 may also be due to scattered light at a flared inner wall of B100.

Although at low SNR, the F410M post-processed image also shows a marginal arc-like feature that is located inside of R1 (labeled as ‘R0?’ in Figure 2), which appears to be collocated with a potential extended feature reported by previous Keck/NIRC2 L' -band observations (labeled as ‘s’ in Guidi et al. 2018). Follow-up observations with higher contrast are needed to confirm the R0 and R2 features, and help to shed light on the morphology of the disk surface.

The F200W image resolves another scattering ring feature in the outermost disk regions (R3, semi-major axis $\sim 3''.5$, width: $\sim 0''.5$; see the middle panel in Figure 2). Tentative evidence for this structure was presented from radial cuts of the disk surface brightness by HST coronagraphic imaging in the optical (Grady et al. 2000; Wisniewski et al. 2008). Rich et al. (2020) revisited this archival data set and better resolved the ring feature. Our NIRCcam observations clearly confirmed this R3 feature. Figure 5 illustrates the radial profiles of the surface brightness around R3 at position angles of 110–130 degrees, showing a $\sim 0''.5$ -wide with a peak at

$\sim 1 - 1.2$ MJy/Sr (note that these radial profiles were not corrected for self-subtraction induced by the ADI reduction). Muro-Arena et al. (2018) modeled the dust profile using detection limits from VLT/SPHERE polarimetric imaging and our result will be useful to further constrain the dust characteristics of the HD 163296 disk.

Pinte et al. (2018) argued that the velocity kink #1 observed with ALMA is collocated with the gap detected with HST in the outer disk (corresponding to R3 in Figure 2; Grady et al. 2000; Rich et al. 2020), but our JWST/NIRCcam map suggests that the kink feature is collocated with the R3 ring itself rather than with the gap. However, as mentioned above, the disk surface is likely flared and the disk regions around R3 could also be flared. Future detailed modeling of the disk-planet interaction will shed light on how the putative planet at kink #1 may interact with the disk and produce features consistent with the observations presented in this work.

3.4. Contrast Limits

We calculated the contrast limits of the JWST/NIRCcam observations using the AnalysisTools modules after masking bright background sources. Negative self-subtraction features are not fully masked, particularly for those at larger separations from the central star and the disk features are not masked either, which increases the noise component and affects the contrast curves.

The azimuthally-averaged radial profiles of the F410M 5σ contrast limits are presented in the left panel of Figure 6, overlaid with the detection limits from the NIRC2 L' - and Ms -band deep coronagraphic observations of HD 163296 (the L' -band observations are from Wallack et al. 2024, and the Ms -band observations are presented in Appendix E). As mentioned in Section 3.2, this method calculates azimuthally-averaged noise values at a given range for the separation from the central star, and this is different from the SNR estimate of the PSF fitting. Particularly at the speckle-dominant separations ($\rho \lesssim 1''.5$) where the residual speckles are not fully azimuthally symmetric, the azimuthally-averaged contrast limit may have overestimated the noise level at a specific position. Therefore we could fit the source candidate that is fainter than the typical F410M contrast limit at $\sim 0''.75$ (star symbol in the left panel of Figure 6). Note that these contrast curves were calculated without deprojecting the disk as the ‘noise’ is attributed by the residual starlight and speckles that are irrelevant to the disk geometry. Our observations achieved a deeper contrast limit than NIRC2 at $\rho \gtrsim 0''.8$ (note that the observational configurations, such as filters, coronagraph specifications, total exposure time, and field rotations, are different).

We also calculated the contrast limits of the F200W data in the same way as the F410M data (see the right panel of Figure 6). Note that the F200W data contain numerous back-

ground stars with bright diffraction patterns as well as negative self-subtraction features (see Figure 1) and it is technically hard to mask all of them when calculating the standard deviation for the noise estimate, making it noisier than the background sensitivity of NIRCam/F200W even outside the regions dominated by speckle noise ($\rho \gtrsim 1''.5$). Previous ground-based high-contrast imaging in the NIR with VLT/SPHERE and Subaru/CHARIS achieved better contrast limits than the F200W data within $1''$ (e.g., Mesa et al. 2019; Rich et al. 2019).

The predicted masses of the putative protoplanets in the HD 163296 system are $\approx 1 - 2 M_{\text{Jup}}$ or smaller (e.g., Liu et al. 2018; Pinte et al. 2018, 2020; Teague et al. 2019) and evolutionary models for these objects (Spiegel & Burrows 2012) predict significantly brighter fluxes at $\sim 4\mu\text{m}$ than at $2\mu\text{m}$. Given the contrast limits derived from our NIRCam observations, the F410M observations are more sensitive to the emission of these planets than the F200W ones. We therefore used the F410M results to estimate upper limits to putative embedded protoplanets and also considered possible circumplanetary disk emission in Section 4.2.

4. DISCUSSION

As outlined in Section 3, our JWST/NIRCam observations detected a compact source candidate at $\approx 0''.75$ from the HD 163296 star in the F410M filter, multiple rings in scattered light in the F200W and F410M filters, and achieved unprecedented contrast limits that allow us to derive upper limits to the mass of putative protoplanets in this system. In this section we discuss in more details the implications of these results.

4.1. Nature of the Point-like Source Candidate

The source candidate detected in F410M (Section 3.2) does not have a counterpart in the F200W map. The contrast limit from the F200W image is $\sim 2 \times 10^{-5}$, corresponding to an apparent magnitude of ~ 16.7 , and the lower limit of the F200W - F410M color is 1.7. Furthermore, previous ground-based observations achieving better contrast levels than the F200W contrast limit (see Section 3.4) did not report any counterpart to the F410W source candidate. Mesa et al. (2019) achieved a contrast limit of $\sim 10^{-6.2}$ in K -band, corresponding to apparent magnitude of ~ 20.3 , and the lower limit of the K - F410M color of this source is ~ 5.3 , suggesting a very red color.

Assuming that this source candidate is a real object, in order to derive the intrinsic magnitude of a source from the measured magnitude one needs to know the extinction in that filter. This is critical for protoplanets that are still embedded in their parent disk, as it has been shown that the dust in the disk can cause very high extinction values even at mid-IR wavelengths for a planet in the midplane which has not

opened a significant gap along its orbit (e.g., Sanchis et al. 2020; Alarcón et al. 2024). The extinction rapidly decreases for planets which are massive enough to clear out the disk material close to their orbit. However, given the large uncertainties on the mass estimates of (putative) young planets, and the intrinsic difficulty in estimating dust opacities and column densities throughout the disk, an estimate of the local extinction from the disk at the location of the putative planet is at this point highly uncertain.

HD 163296 does not show any significant extinction ($A_V = 0$; Rich et al. 2019). If an embedded planet has cleared out the disk around its orbit so that light from the planet is not extinguished by the surrounding disk materials, our measured magnitude at F410M (see Fig. 9 with $\Delta F_{410M} = 11.8$ mag) would correspond to a hot-start $\approx 2 - 4 M_{\text{Jup}}$ giant planet (Spiegel & Burrows 2012). These planet mass estimates would be lowered if part of the measured flux originates from a circumplanetary disk (CPD) surrounding the putative planet. For example, as detailed in Section 4.2.2, according to the CPD models by Zhu et al. (2018), the measured contrast level would correspond to a warm/cold-start accreting planet with the product between planet mass and mass accretion rate of $\approx 6 \times 10^{-6} M_{\text{Jup}}^2/\text{yr}$, with a CPD with an inner radius of $\approx 1 R_{\text{Jup}}$.

We note that, depending on the disk properties (e.g., viscosity) massive planets would likely perturb the gas and dust in the disk ($> 10\%$ of Keplerian motion, corresponding to $\gtrsim 2 M_{\text{Jup}}$ planets at a few tens of au; Pinte et al. 2020). Under the assumption that this source is a real planet embedded in the midplane of the disk, the deprojected stellocentric separation corresponds to ~ 111 au, just outside B100 (see Figure 4). The separation of the source candidate coincides with a dip in the radial profile of the ^{12}CO emissions (Figure 8, see also Appendix F for the comparison with the CO map), which is likely due to a local decrease in the gas density of the disk. A future detailed analysis of the disk-planet interaction using hydrodynamic numerical models can shed more light on the possible perturbations induced by this object on the disk, as well as on the expected extinction due to the disk material at the location of the source candidate.

In another scenario in which no local perturbation to the disk is present, Alarcón et al. (2024) derived a very high extinction value of $A_{F410M} \sim 25 - 30$ mag at the location of our source candidate (see also Section 4.2 for the model assumptions and caveats). If true, this would make the intrinsic luminosity at $4\mu\text{m}$ of this source even higher than the central star, and it would make very unlikely also the scenario of a background object for the nature of this source.

Even though the source candidate is detected with a robust SNR at small KL modes, however, it is still possible that this feature is actually false positive after averaging. Due to the NIRCam diffraction patterns, extended feature like R1 could

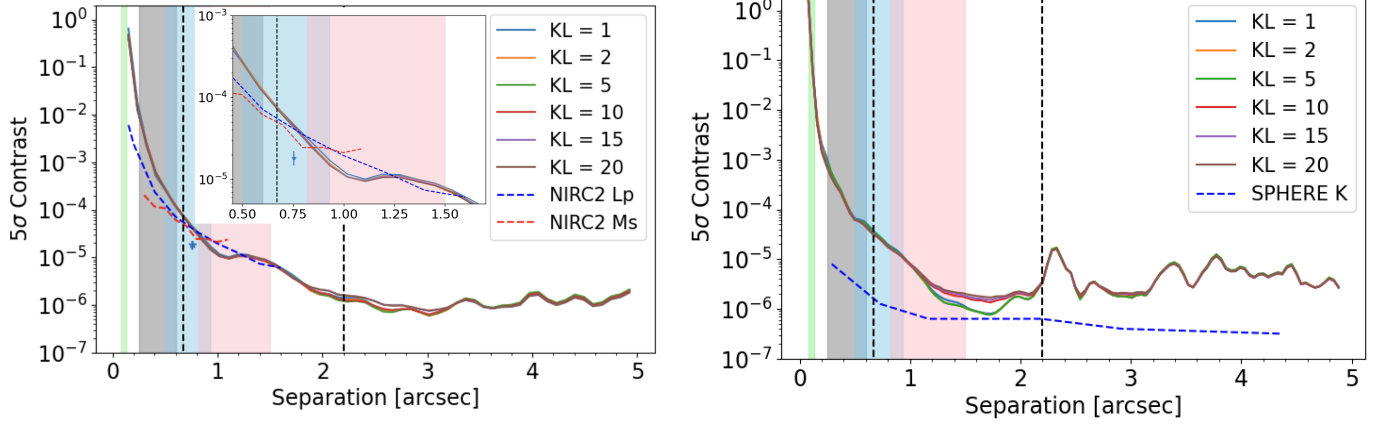


Figure 6. Left) 5σ contrast limits of the F410M data overlaid with Keck/NIRC2 contrast limits (L' -band; Wallack et al. 2024, Ms -band; this study, see Appendix E). The insert panel is a zoomed-in version of the contrast limits at separations from the central star around $1''$. The star symbol indicates the contrast and separation of the source candidate from the F410M data. The vertical dashed black lines indicate the separations of the ALMA velocity kinks. The light-green, gray, sky-blue, and pink shaded areas correspond to the projected separation ranges of the ALMA dust gaps (D10, D45, D86, and D145, respectively; Huang et al. 2018; Isella et al. 2018). Right) The contrast limits obtained from the F200W data overlaid with a rough SPHERE 5σ contrast limit we inspected visually from Mesa et al. (2019), where we applied the disk inclination to the separations for the consistency with our contrast limits.

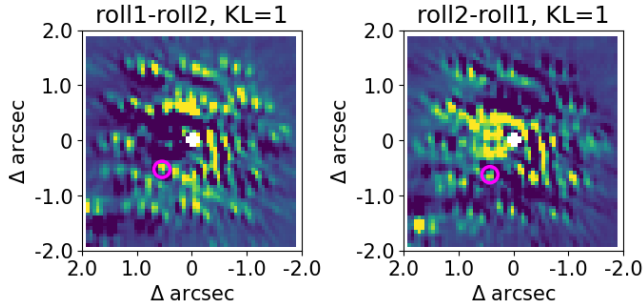


Figure 7. Comparison of roll-subtracted images at each roll at $KL=1$. The magenta circle indicates the location of the source candidate. Note that the north position angle of each image is not corrected.

introduce a point-like feature at different locations, but our forward modeling test with the toy model presented in Appendix D did not reproduce such a bright and stable feature at the location of the source candidate. Therefore we do not consider this scenario hereafter.

We also investigated intermediate files of roll-subtracted images at each roll state to investigate the possibility of a residual speckle or a hot/bad-pixel cluster. If there was a bright feature at either of the roll-subtracted images, it suggests that the feature is likely a variable speckle or a hot/bad pixel cluster. If such feature appears at both roll-subtracted images, it suggests real astronomical source. Figure 7 shows the combined roll-subtracted images and we did not recognize significant excesses suggesting such false positives at the location of the source candidate we detected. However, we also did not confirm the stable signal there because each of the roll-subtracted state images has noisier speckle residuals than the final processed image.

In summary, the extracted color and location relative to the HD 163296 disk suggests that this source candidate is intriguing if it is a real astronomical source, but because of technical difficulties of our data, we defer the conclusion of this identity to follow-up observations with a higher contrast or future analysis with RDI reduction when reference PSFs in the same observational configurations are available.

4.2. Constraining the Mass of the ALMA Putative Planets

4.2.1. Comparison with Evolutionary Models

We derived upper limits for the mass of the putative planets at the locations of the ALMA velocity kinks (#1 at $\rho = 2''/2$ and #2 at $0''.67$; Pinte et al. 2020) and dust gaps, with the exception of the D10 gap (light-green in Figure 6), which is located inside the inner working angle of the NIRCcam observations. Following the theoretical predictions for the mass of these putative protoplanets, in Figure 9 we converted the NIRCcam F410M contrast limits into mass limits using the Spiegel & Burrows (2012) evolutionary models for young planets with masses between 1 and $4 M_{\text{Jup}}$. These models also account for varying initial entropy (hot-/warm-/cold-start models; Spiegel & Burrows 2012), different assumptions on the composition of the planetary atmosphere (cloud-free spectra and hybrid-clouds spectra at solar metallicity; Burrows et al. 2011), and varying planetary ages, taken to be between 1 and 5 Myr for the HD 163296 system.

The sky-blue and pink shades in Figure 9 illustrate the converted mass limits for planets inside the projected separation ranges of the D86 and D145 gaps, respectively (following the same shades as in Figure 6). The detection limit at a specific position depends on the position angle around the central star, and we investigated the empirical detection limit

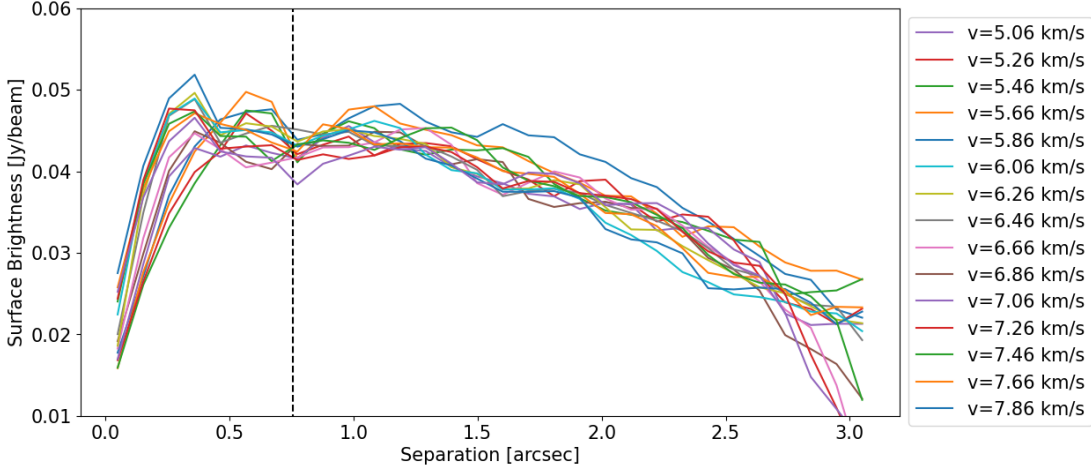


Figure 8. Radial profiles of the South West side of the ^{12}CO gas emissions at $v = 6.46 \pm 1.4$ km/s (see Appendix F). The vertical dashed line indicates the separation of the source candidate.

by injecting fake sources with varying magnitude based on the 5σ contrast curves (Section 3.4). We focused on constraining the flux of the putative planets at the ALMA velocity kinks. At these locations, we derived the contrast limits of $\approx 8.3 \times 10^{-7}$ ($\Delta F_{410\text{M}} = 15.2$ mag) for kink #1 and $\approx 3.3 \times 10^{-5}$ ($\Delta F_{410\text{M}} = 11.2$ mag) for #2, respectively (see Appendix G). The derived detection limit at kink #2 is different from the numerical contrast curve at the same separation (6.9×10^{-5} at $0''.67$) by a factor of ~ 2 due to the presence of the R1 ring at similar separations. The derived $F_{410\text{M}}$ contrast limits correspond to a $\sim 1 - 2 M_{\text{Jup}}$ hot-/warm-start gas giant at ~ 5 Myr and a $4 M_{\text{Jup}}$ hot-start object at ~ 1 Myr at kink #1 and #2, respectively.

Note that these estimates were obtained by assuming $A_V = 0$, which is the estimated extinction for the star. As for the case of the source candidate discussed in the previous section, if the light of these putative planets is affected by significant extinction caused by the disk, the upper limit would be much higher. For example, the models presented by Alarcón et al. (2024) provided estimates of $A_{F_{410\text{M}}} \sim 13$ mag for the putative planet at the kink #1 (private communication) and of ~ 39 mag for the other planet at kink #2. However, these models do not account for any perturbation on the disk material at the kink #1 location, and the planet considered for their modeling at the kink #2 has a very low mass of $0.1 M_{\text{Jup}}$. If these planets are more massive, their interaction with the disk would likely remove a significant fraction of the disk material close to their orbits, and that would strongly decrease the estimated extinction. In fact, significantly lower values for the extinction can be obtained from the optical depths derived at $\lambda \approx 1$ mm from the analysis of the ALMA observations presented in Isella et al. (2016, 2018) (cf. Guidi et al. 2022). However, converting those optical depths into an extinction in the NIR/mid-IR requires an extrapolation over almost two orders of magnitude in wavelength and would be highly un-

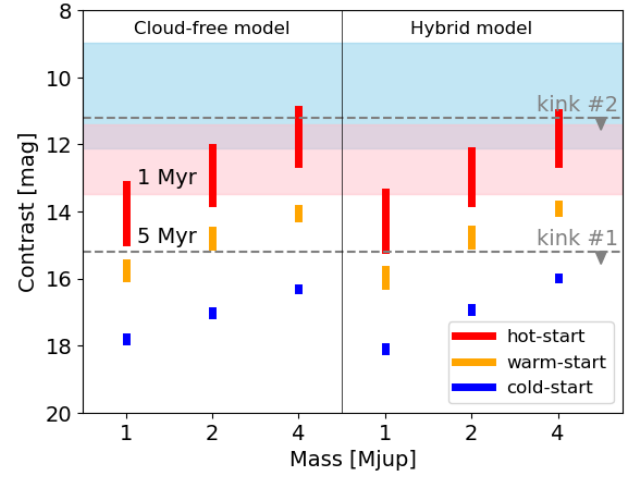


Figure 9. Diagram showing the conversion between the contrast limits in the $F_{410\text{M}}$ filter and the corresponding predicted contrast from evolutionary models of young giant planets with different properties. The dashed horizontal lines indicate the $F_{410\text{M}}$ empirical detection limits at the location of the ALMA velocity kink #1 ($\Delta F_{410\text{M}} = 15.2$ mag) and #2 ($\Delta F_{410\text{M}} = 11.2$ mag), respectively. The colored shades indicate the contrast limits at the projected separations of the ALMA dust gaps (sky-blue for D45 and pink for D86, as in Figure 6). We took into account hot- (red)/warm- (orange)/cold-start (blue) evolutionary models (Spiegel & Burrows 2012) with cloud-free and hybrid clouds atmospheres at solar metallicity (Burrows et al. 2011, see text for details), ages between 1 and 5 Myr (the upper and lower limits of each model range correspond to 1 and 5 Myr, respectively), and assuming the same extinction as the central star, i.e. $A_V = 0$.

certain. Future modeling work that incorporates these embedded planets is needed to derive more accurate extinction estimates at those specific locations.

4.2.2. Incorporating Circumplanetary Disk Models

We took into account possible thermal emission from a CPD around the putative young planets. We added the emis-

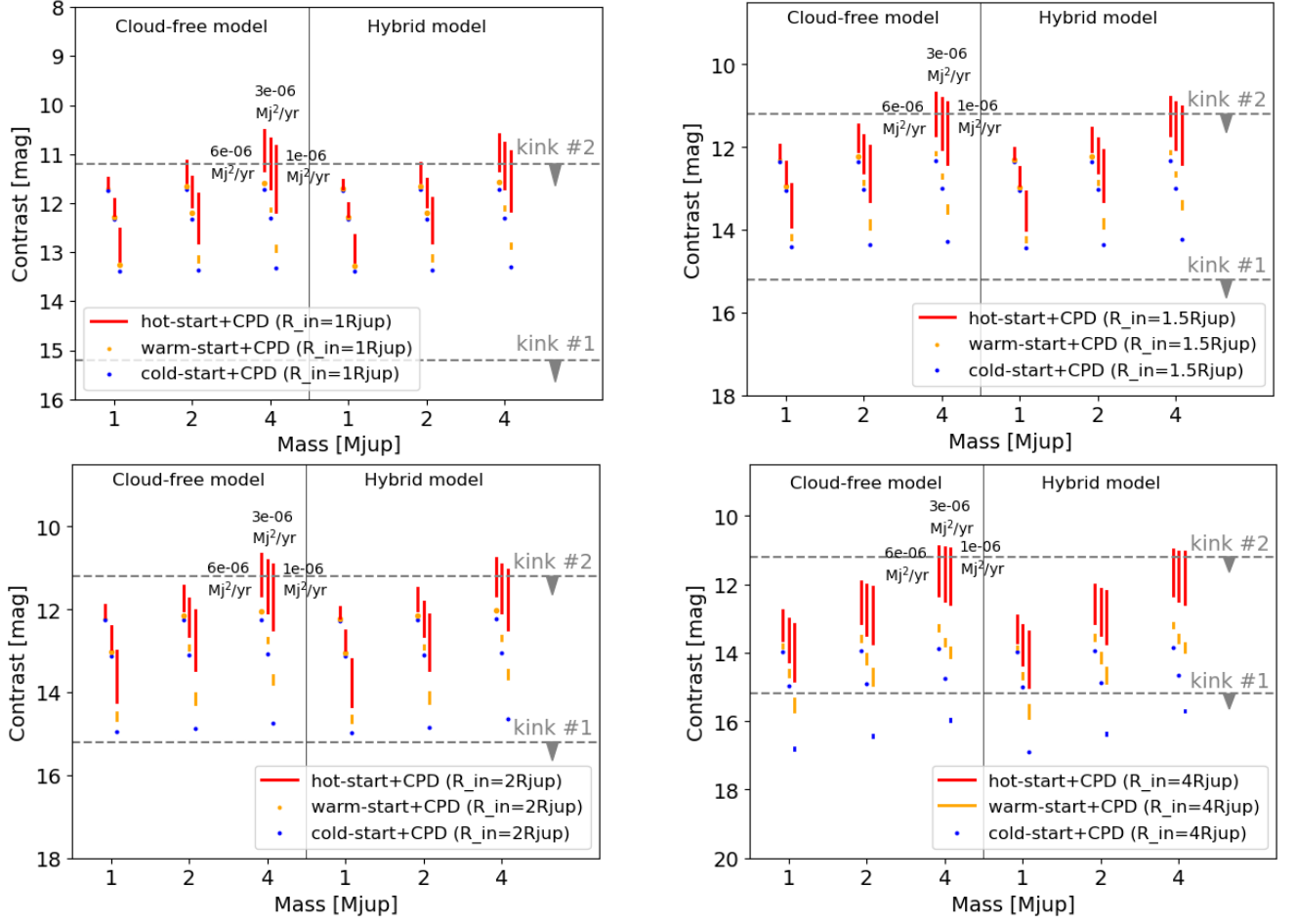


Figure 10. Same as in Figure 9 with the addition of accreting CPD models (Zhu 2015), calculated with different values for the disk inner radius ($R_{\text{in}} = 1, 1.5, 2, 4 R_{\text{Jup}}$, from top left to bottom right panels, respectively), and for the product of planet mass and mass accretion rate ($M_{\text{p}} \dot{M} = 1, 3, 6 \times 10^{-6} M_{\text{Jup}}^2/\text{yr}$; for the order, see the annotations next to the data points of the $4 M_{\text{Jup}}$ cloud-free model).

sion predicted by the Zhu (2015) accreting CPD models to the hot-/warm-/cold-start models (Spiegel & Burrows 2012) presented in the previous section. The comparison between these planet+CPD model predictions and our detection limits derived at the location of the two ALMA velocity kinks is shown in Figure 10 (the planet models are the same as in Figure 9). For the CPD models, we considered ranges for the product between planet mass and mass accretion rate ($M_{\text{p}} \dot{M} = 1 - 6 \times 10^{-6} M_{\text{Jup}}^2/\text{yr}$ assuming a planet forming within the stellar age), for the CPD inner radius ($R_{\text{in}} = 1 - 4 R_{\text{Jup}}$), and a CPD disk inclination of $i = 47^\circ$, which assumes coplanarity with the protoplanetary disk.

Except for the case of a CPD with a relatively large inner radius $R_{\text{in}} = 4 R_{\text{Jup}}$, the F410M detection limit at kink #1 rules out a CPD model around a planet with mass $\geq 1 M_{\text{Jup}}$. A lower mass accretion rate than the values considered here would be required to have a warm- or cold-start $1 M_{\text{Jup}}$ planet surrounded by a CPD with a total flux consistent with our F410M detection limit.

5. CONCLUSION

We carried out JWST/NIRCam coronagraphic observations of the HD 163296 system with the F410M and F200W filters to search for infrared emission from the putative young planets predicted by models of the disk+planet interaction. We employed roll-subtraction ADI reduction at two roll positions and utilized the spaceKLIP pipeline to remove stellar PSF. After deliberate calibrations and post-processing, we did not detect robust signals of embedded protoplanets at the locations of the disk substructures observed with ALMA. We detected numerous background sources within the FoV, and several arc features that are likely tracing the forward-scattering side of more extended rings in the disk (R0–R3). Especially in the F200W we found an evident difference in the number density of background sources between regions within and beyond R3, which indicates significant extinction of the light from background sources by dust in the protoplanetary disk.

We also found a point-like source candidate at a separation $\rho \approx 0''.75$ from the central star that is detected only in the F410M band at an SNR $\approx 4 - 5$ at KL=1–4 with a contrast of $\Delta F410M=11.8$ mag. This corresponds to an apparent magnitude in the F410M band of 16.42 ± 0.15 mag and to a lower limit for the F200W-F410M color of 5.5 referring to the previous VLT/SPHERE *K*-band observations. The measured flux is consistent with the predicted flux of models of young planets with a mass $\approx 2 - 4 M_{\text{Jup}}$ without significant extinction from the disk material.

We estimated contrast limits using spaceKLIP modules to derive upper limits for the mass of the putative young planets. Our F410M data achieved unprecedented azimuthally-averaged contrast limits at $\sim 4\mu\text{m}$ at $\rho \gtrsim 0''.8$. In particular, we compared the NIRCam detection limits at the locations of the ALMA velocity kinks, where $\sim 1 - 2 M_{\text{Jup}}$ planets are predicted, with the predictions from evolutionary models for planets with different initial entropies (hot-/warm-/cold-start models, Spiegel & Burrows 2012), with or without a circumplanetary disk. We found that the non-detection at kink #1 requires 1) extinction by the disk and/or 2) cold or warm-start formation with a moderate accretion rate ($\dot{M}_{\text{p}} \lesssim 1 \times 10^{-6} M_{\text{Jup}}^2/\text{yr}$). Less stringent constraints were obtained on the mass of the putative planet causing the ALMA velocity kink #2.

Follow-up observations and detailed modeling of the HD 163296 system are essential to confirm the nature of the point-like source candidate, and establish its membership to the system, as well as to investigate the disk morphology, extinction, and planet-disk interaction in detail. Significant improvements are expected in the contrast limits that can be achieved with JWST in the future through RDI, including efforts to make empirical corrections on synthesized reference PSFs (Lawson et al. 2024), when reference stars will be available in the same configuration as our data.

Finally, we caution future direct imaging plans aiming at embedded protoplanets to acknowledge the risk of the potential extinction due to the protoplanetary disk. Observing (face-on) disks with a large cavity (e.g., PDS 70) or utilizing longer wavelengths, for instance, JWST/MIRI (Cugno et al. in prep) and future instruments/concepts such as Mid-infrared ELT Imager and Spectrograph (METIS; Brandl et al. 2010) mounted on the European Extremely Large Telescope (E-ELT), Mid-Infrared Camera, High-disperser, and IFU (MICH; Packham et al. 2012) or Planetary System Imager (PSI; Fitzgerald et al. 2019) on the Thirty Meter Telescope (TMT), Thermal Infrared imager for the GMT which provides Extreme contrast and Resolution (TIGER; Hinz et al. 2012) on the Giant Magellan Telescope (GMT), Planet Formation Imager (PFI; Monnier et al. 2014), and Large Interferometer For Exoplanets (LIFE; Quanz et al. 2022) could lower the risk of non-detections or insufficient sensitivities due to

the disk extinction. Searching for CPDs at millimeter wavelengths would also be useful to advance the understanding of planet formation mechanisms (e.g., with the Next Generation Very Large Array; Ricci et al. 2018; Zhu et al. 2018).

ACKNOWLEDGMENTS

The authors would like to thank the anonymous referee for their constructive comments and suggestions that improved the quality of the paper. We thank Vanessa Bailey and Cornelis Dullemond for contributing to the JWST proposal (ID: GO 2540, PI: Luca Ricci). We are grateful to Jorge Llop-Sayson for helping with synthetic RDI reduction, William Balmer for useful comments on the spaceKLIP steps, Felipe Alarcon for providing model extinction maps of the HD 163296 disk with the NIRCam filters, Gabriele Cugno for comprehensive discussions about JWST data, and Maxwell Millar-Blanchaer for his comments on the disk forward modeling.

This work is based on observations made with the NASA/ESA/CSA James Webb Space Telescope. The data were obtained from the Mikulski Archive for Space Telescopes at the Space Telescope Science Institute, which is operated by the Association of Universities for Research in Astronomy, Inc., under NASA contract NAS 5-03127 for JWST. These observations are associated with program GO 2540. The specific observations analyzed in this work can be accessed via <https://doi.org/10.17909/j87q-jf82>. Part of data presented here were obtained at the W. M. Keck Observatory, which is operated as a scientific partnership among the California Institute of Technology, the University of California and the National Aeronautics and Space Administration. The Observatory was made possible by the generous financial support of the W. M. Keck Foundation. We wish to acknowledge the critical importance of the current and recent Mauna Kea Observatory daycrew, technicians, telescope operators, computer support, and office staff employees, especially during the challenging times presented by the COVID-19 pandemic. Their expertise, ingenuity, and dedication are indispensable to the continued successful operation of these observatories. The authors wish to recognize and acknowledge the very significant cultural role and reverence that the summit of Maunakea has always had within the indigenous Hawaiian community. We are most fortunate to have the opportunity to conduct observations from this mountain. This work has made use of data from the European Space Agency (ESA) mission *Gaia* (<https://www.cosmos.esa.int/gaia>), processed by the *Gaia* Data Processing and Analysis Consortium (DPAC, <https://www.cosmos.esa.int/web/gaia/dpac/consortium>). Funding for the DPAC has been provided by national institutions, in particular the institutions participating in the *Gaia* Multilateral Agreement. This publication makes use of VOSA, developed under

the Spanish Virtual Observatory (<https://svo.cab.inta-csic.es>) project funded by MCIN/AEI/10.13039/501100011033/ through grant PID2020-112949GB-I00. VOSA has been partially updated by using funding from the European Union’s Horizon 2020 Research and Innovation Programme, under Grant Agreement n° 776403 (EXOPLANETS-A).

Support for program GO 2540 was provided by NASA through a grant from the Space Telescope Science Institute, which is operated by the Association of Universities for Research in Astronomy, Inc., under NASA contract NAS 5-03127. Part of this research was carried out at the Jet Propul-

sion Laboratory, California Institute of Technology, under a contract with the National Aeronautics and Space Administration (80NM0018D0004). A.I. acknowledges support from the National Aeronautics and Space Administration under grant No. 80NSSC18K0828. S.Z. acknowledges support by NASA through the NASA Hubble Fellowship grant #HST-HF2-51568 awarded by the Space Telescope Science Institute, which is operated by the Association of Universities for Research in Astronomy, Inc., for NASA, under contract NAS5-26555.

APPENDIX

A. COMPARISON OF THE TWO MASKS WITH THE F410M FILTER

Figure 11 compares the post-processed images obtained from the primary data with F410M/MASK430R and the by-product data with F410M/MASK210R, as described in Section 2. The F410M/MASK430R image was taken with the larger mask, and it suppresses residual speckles better than the other by-product data. Note that the PSF core of the central star in the MASK210R data set is saturated (showing NaN in the data), and spaceKLIP replaces the NaN value with 0 before image registration, which induced artifact features (marginal cross ripples). We reduced both data sets in the same manner and did not treat saturated pixels in the MASK210R data.

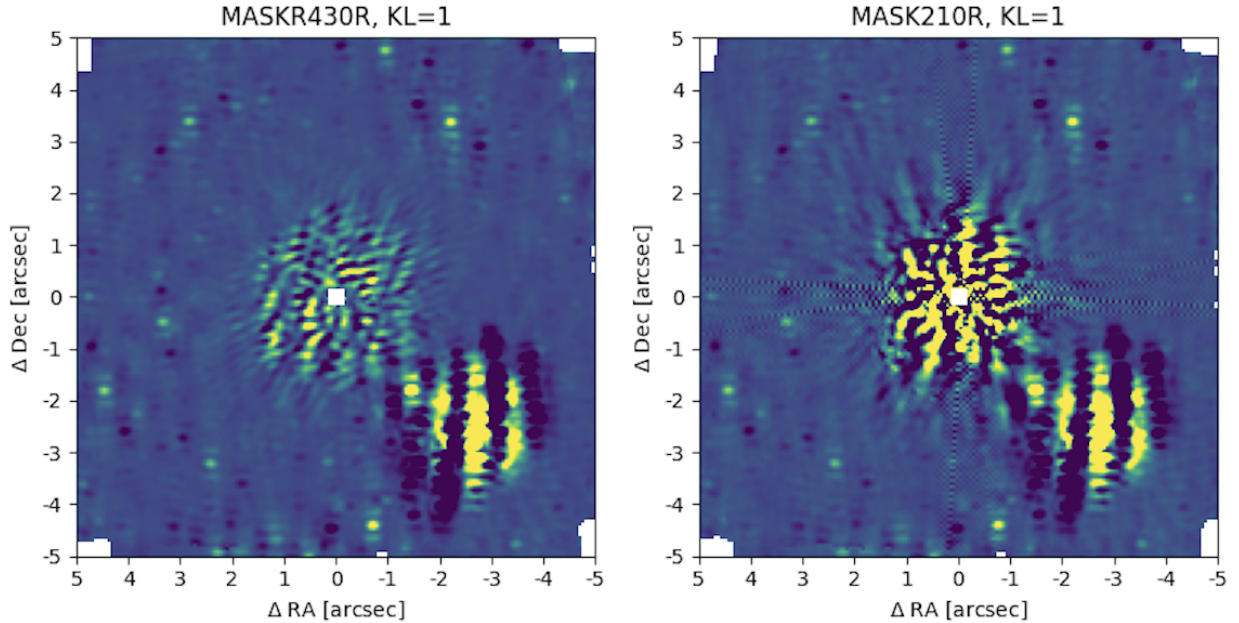


Figure 11. Comparison of the post-processed images of the primary mask (left) and the by-product data for the F410M filter (right) in the same color scale.

B. POST-PROCESSING AND FORWARD MODELING OF THE F410M DATA AT DIFFERENT KL MODES

Figure 12 shows the results of our ADI post-processing tests using KL values between 1 and 30. We found that more aggressive strategies for PSF subtraction with $KL > 10$ do not greatly change the outcome of the post-processing images.

Figure 13 shows some examples of PSF fitting at different KL modes. As mentioned in Section 4.1, aggressive PSF subtraction at $KL \geq 5$ attenuates the signal of the source candidate as the angle offset between the two roll states is just $\sim 10^\circ$.

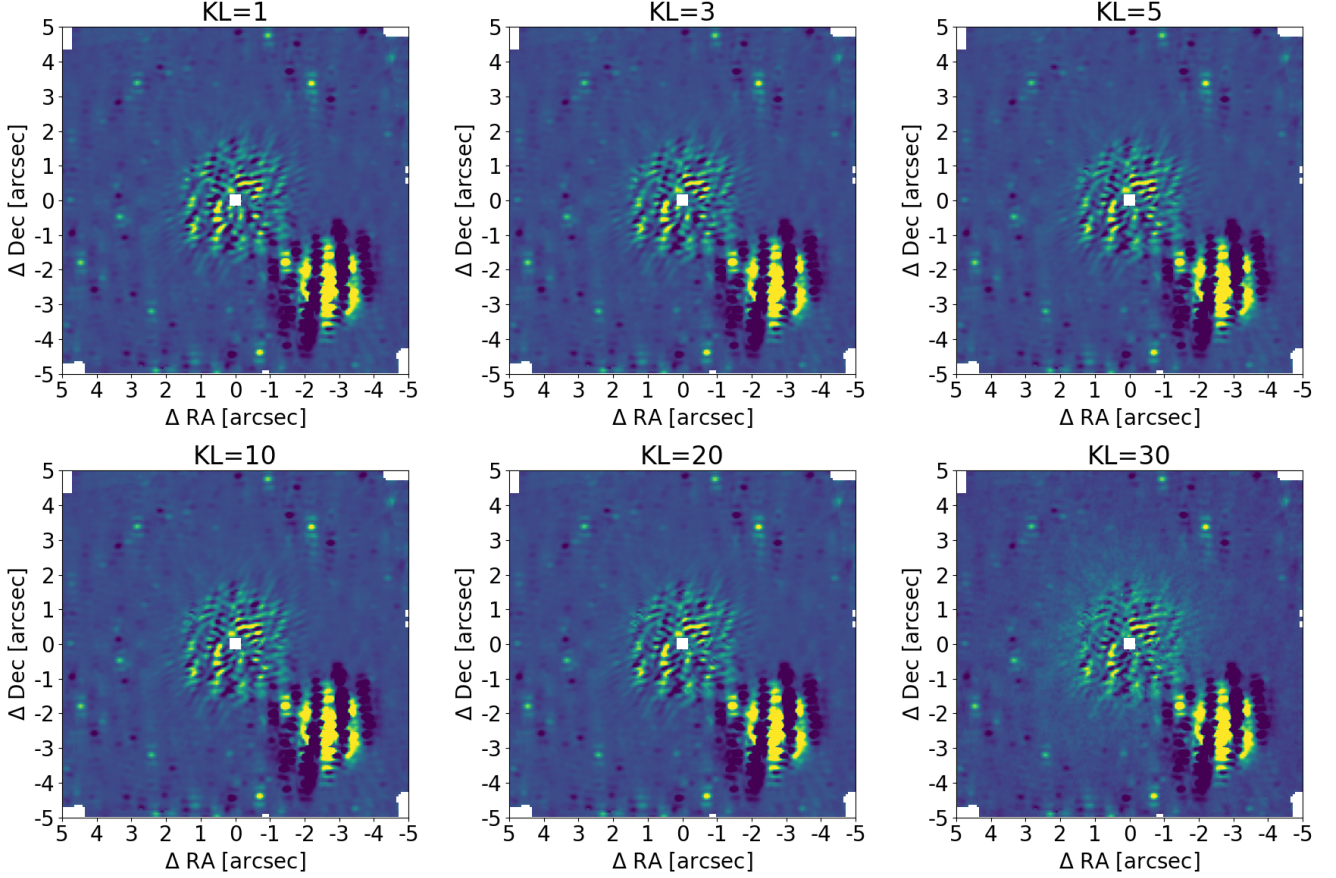


Figure 12. Gallery of the ADI post-processed images obtained with different KL modes, as labeled above each image.

C. ATTEMPT AT RDI WITH A SYNTHESIZED WEBBPSF

For JWST coronagraphic imaging, RDI is generally more efficient than ADI in detecting companions (Carter et al. 2023; Hinkley et al. 2023), but it is hard to find a suitable reference star that has a similar color to a young star with a disk. Our program did not observe a reference star, and we attempted synthetic RDI by generating reference PSFs via WebbPSF (Greenbaum et al. 2023). We incorporated the wavefront errors measured on the closest date of our observations and with the same instrumental configurations. However, the synthetic PSFs we generated in this way proved to be not optimal for RDI post-processing as shown in Figure 14, where strong speckle residuals and several over-subtraction features are evident in both filters.

D. FORWARD MODELING OF THE DISK FEATURES

As described in Section 3.3 we tested forward modeling using a toy disk model to interpret the F410M post-processed image. We refer to Rich et al. (2019) for a model for the R1 ring, and slightly modified the inner and outer edges and the offset from the star to better match the arc-like feature seen in the F410M image. A second partial ring was added to the model to reproduce the R2 feature, as well as to test if additional arc-like features in the F410M map can be reproduced. Before running forward-modeling modules, we convolved the toy model with an off-axis WebbPSF, in the same way as in Appendix C, and applied the mask throughput map, which was modeled with the spaceKLIP processes. Note that the actual NIRCam PSF shape near the coronagraph mask is a function of separation from the mask center, and detailed disk modeling requires convolving the model with on-axis PSFs (e.g., Leisenring 2025). We finally used the Disk Forward Modeling modules in pyklip (DiskFM; Mazoyer et al. 2020) for forward modeling. Figure 15 presents our toy model, a WebbPSF-convolved and mask throughput-applied disk image, and the resulting map for the forward-modeled disk, which simulates the post-processing methods applied to our JWST/NIRCam observations in the F410M filter. Figure 16 is a gallery of the forward-modeled disk at different KL modes. We found that these bright disk features introduce some local excesses at different locations from the rings (e.g., some relatively bright pixels in the

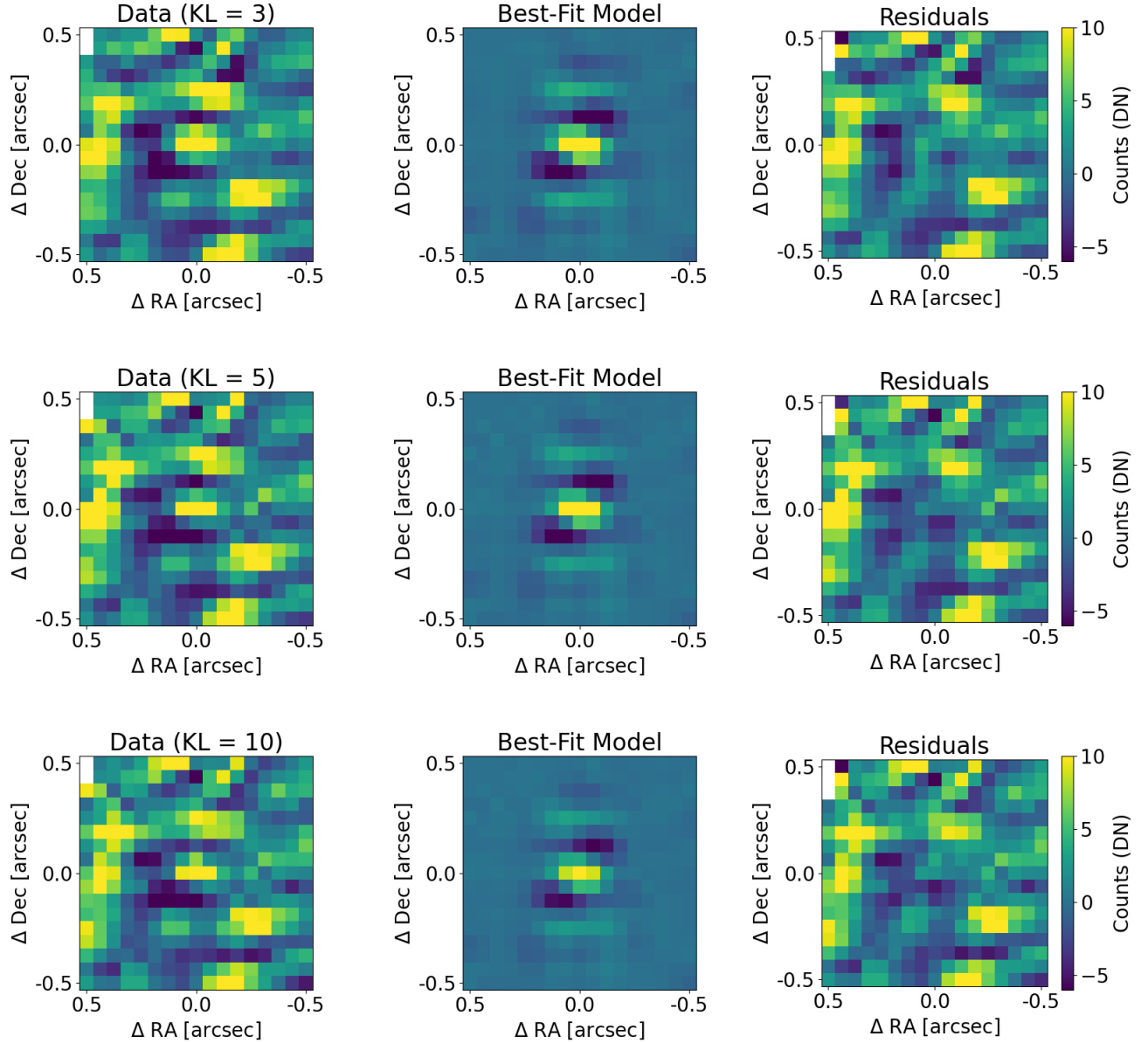


Figure 13. PSF fitting results (see Figure 3) at KL = 3, 5, and 10 (from top to bottom).

south-west side from the star), but they are not stable among different KLs. Furthermore, we did not detect additional extended features than what we modeled, suggesting that the R2 feature is not induced by diffraction patterns of produced by the R1 ring.

E. KECK/NIRC2 M_S -BAND OBSERVATIONS

JWST and ground-based coronagraphic observations play complementary roles for the search for companions. At inner separations (extreme) adaptive optics combined with optimized coronagraphs have achieved higher contrast than JWST coronagraphy (e.g., Ren et al. 2023) while JWST can achieve very high sensitivity at larger separations.

In this study we reduced archival Keck/NIRC2 M_S -band (pivot wavelength: $\lambda = 4.670 \mu\text{m}$, bandwidth: $\Delta\lambda = 0.241 \mu\text{m}$) data (PI: Garreth Ruane, date: 2020 August 10 UT, total exposure time: 7500 seconds). The data were taken with the vortex coronagraph (Serabyn et al. 2017) and vertical angle mode for ADI. After calibrating the raw data (flat fielding, distortion correction, sky subtraction, image alignment), we cropped the image by $\sim 2''.5 \times 2''.5$ focusing on inner separations, where Keck/NIRC2 can outperform JWST/NIRCam high-contrast imaging (see also Section 3.4 for the practical contrast limits), and

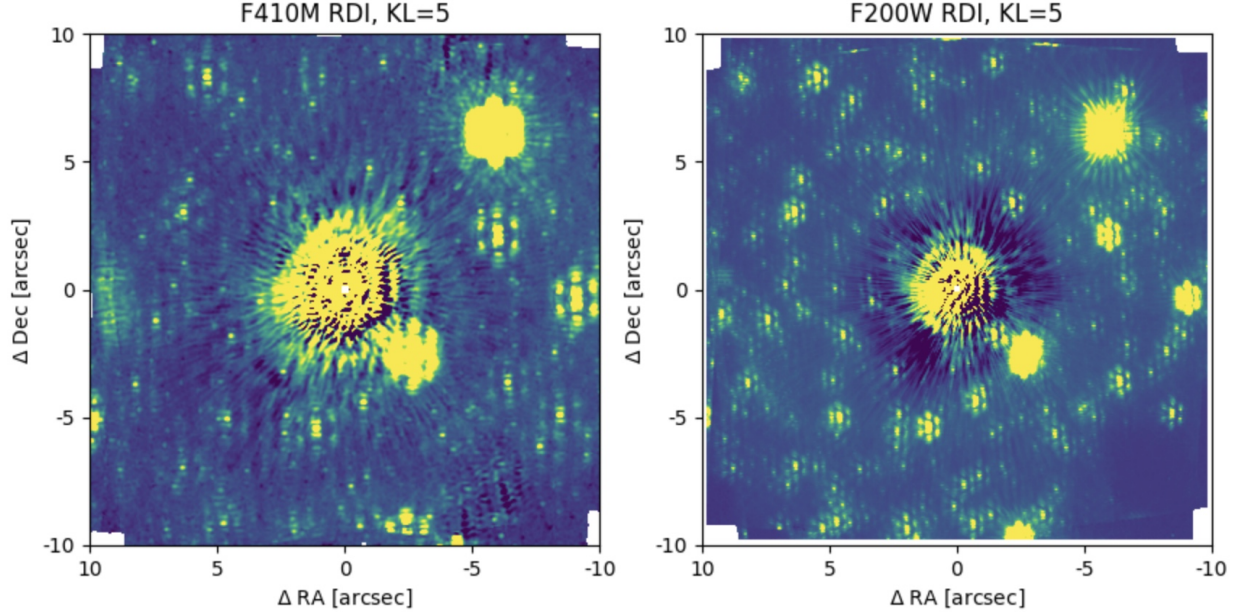


Figure 14. RDI post-processed images in the F410M filter (left) and F200W filter (right) after generating synthesized reference PSFs from WebbPSF, and incorporating the wavefront errors close to the observing epoch and the observational configurations. Note that we conducted RDI with the full FoV in each filter. The inner regions at separations smaller than $3''.5$ are dominated by residual speckles and artifacts by the modeled reference PSF.

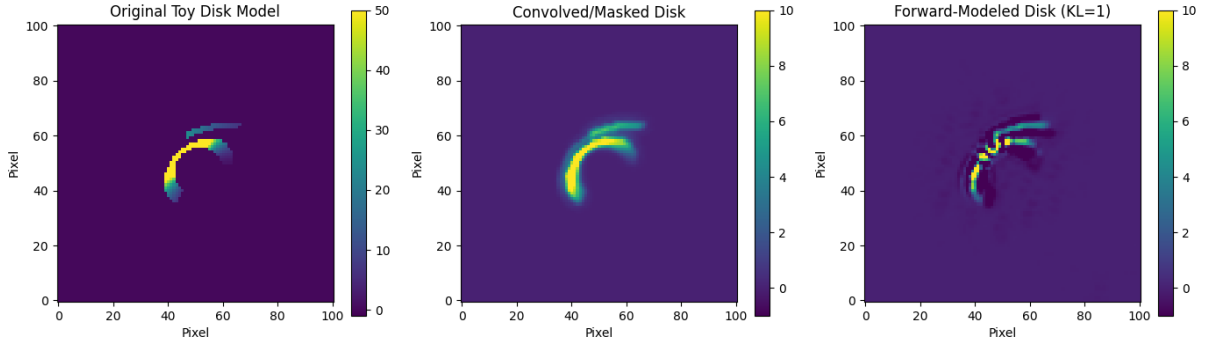


Figure 15. Comparison between the image of the toy disk model presented in Appendix D (left), the model image after convolution using WebbPSF at F410M and MASK430R throughput (middle) and a forward-modeled disk, which simulates the post-processing methods applied to our JWST/NIRCam observations in the F410M filter (right, KL=5). The forward-modeled image suggests that the bright disk feature convolved with WebbPSF can introduce point-like diffraction patterns at different locations from the disk feature (e.g., bright pixels at the lower right in the right panel) but does not introduce significant additional extended features.

then utilized `pyklip` post-processing algorithms to perform ADI reduction. The left panel in Figure 17 shows the post-processed NIRC2 image with a clear detection of R1 and a marginal detection of R2.

As described in Section 3.4, at separations $\rho \lesssim 0''.8$ covering the ALMA dust gaps D45 and D86, the Keck/NIRC2 observations achieved a better contrast level than the NIRCam/F410M observations. However, the NIRC2 contrast limits did not achieve enough contrast to be sensitive to planets with masses $\lesssim 5 M_{\text{Jup}}$ at the D45 and D86 locations (see the right panel in Figure 17). In contrast, the F410M data achieved better mass limits than the NIRC2 data in the D86 gap as well as at larger separations (see Section 4.2).

We also note that at the location of the source candidate discussed in Section 4.1, the NIRC2 data did not reach enough contrast to detect this source. We injected fake sources assuming the same contrast level to the F410M data (1.83×10^{-5}) at the same separation ($0''.754$) and at four position angles in the data set and reran the `pyklip` reduction, but did not reproduce the injected sources.

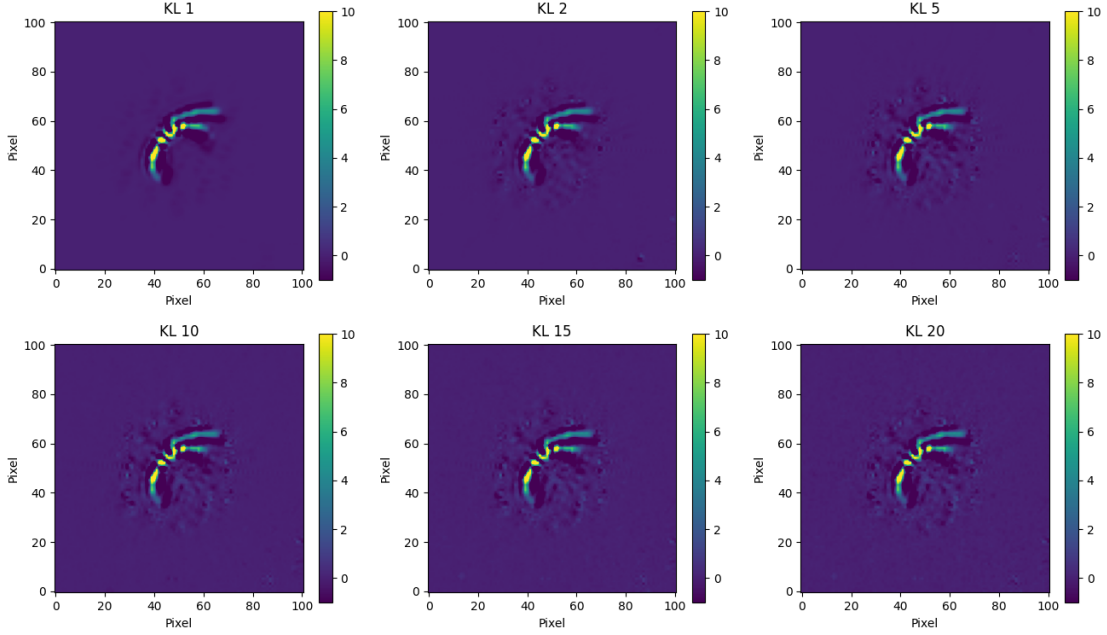


Figure 16. Gallery of the forward-modeled disk (Figure 15) with different KL modes.

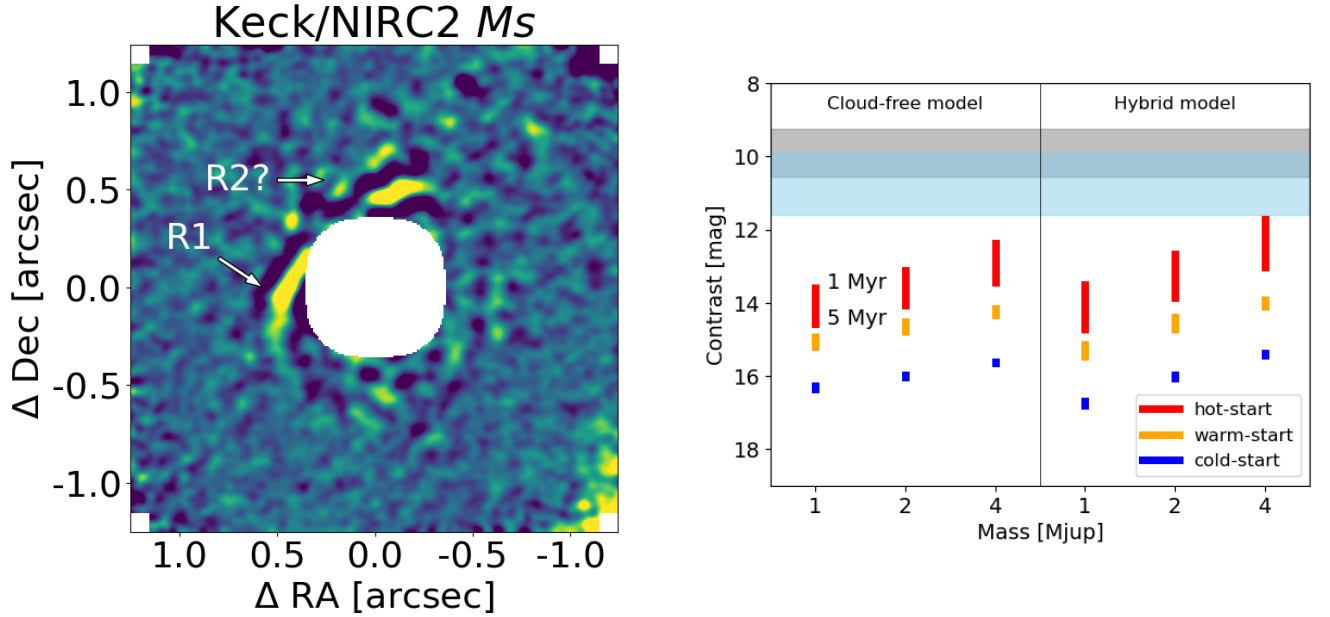


Figure 17. Left) Keck/NIRC2 M_s -band post-processed image after smoothing with a Gaussian with $\sigma = 2$ pix to better highlight the extended features. Right) Diagram showing the conversion between the NIRC2 M_s -band contrast limits and the mass from evolutionary models of planets with different properties (as in Figure 9; the colored shades indicate the contrast limits at the projected separations of the ALMA dust gaps (gray for D10 and sky-blue for D45); the colored bars represent the hot- (red)/warm- (orange)/cold-start (blue) models (Spiegel & Burrows 2012) with cloud-free and hybrid clouds atmospheres at solar metallicity (Burrows et al. 2011), and ages between 1 and 5 Myr (the upper and lower limits of each model range correspond to 1 and 5 Myr, respectively), assuming the same extinction as the central star, i.e. $A_V = 0$.

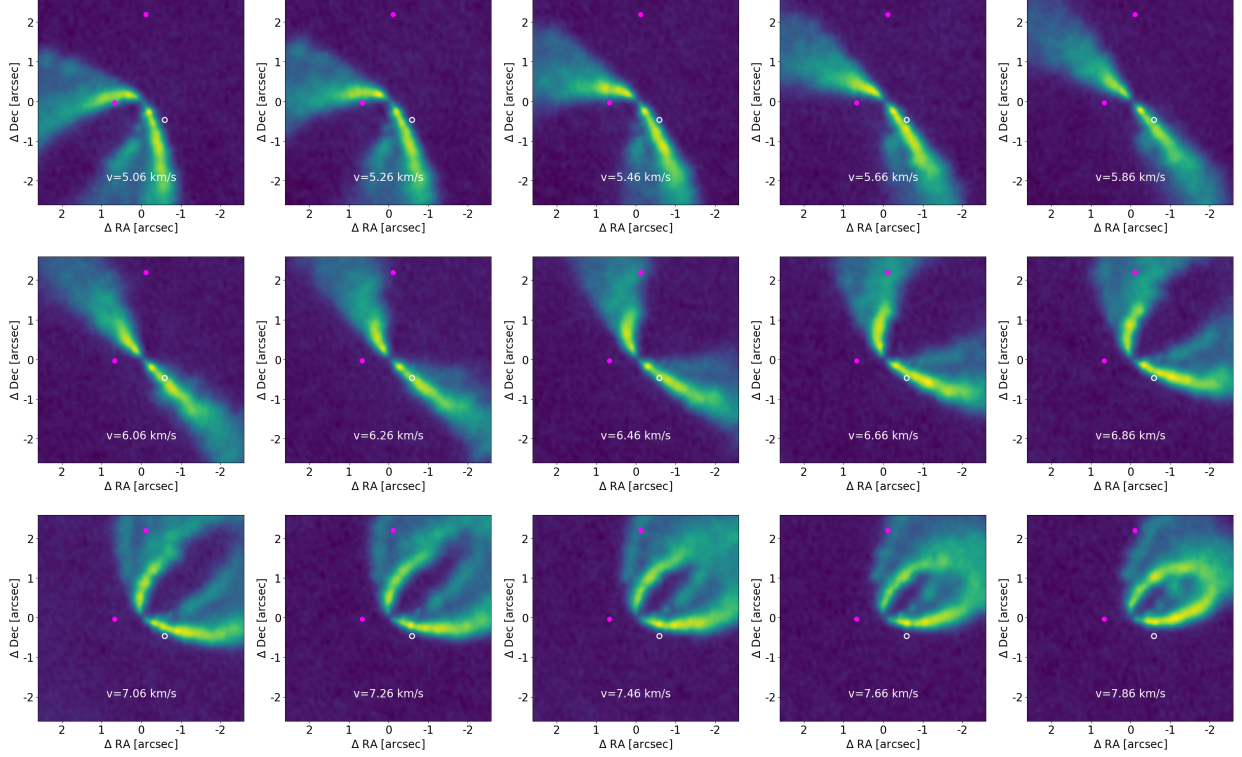


Figure 18. Comparison of the source candidate (white) as well as the velocity kinks (magenta) with the ^{12}CO ($J = 2 - 1$) channel maps obtained by MAPS (FWHM of the beam size: $0''.15$; Öberg et al. 2021).

F. ALMA CO VELOCITY MAPS

We downloaded the ALMA ^{12}CO ($J = 2 - 1$) molecular gas emission data of HD 163296 from the MAPS webpage³, which has a higher velocity resolution than the DSHARP CO data (Isella et al. 2018). Figure 18 shows the location of the source candidate detected in the NIRCam/F410M data (see Section 4.1) on the ALMA channel maps. Figure 8 in the main text shows a comparisons of the radial profiles of the CO gas emissions with the separation of the source. As mentioned in Izquierdo et al. (2023), the ^{12}CO emissions have a dip at a similar separation to the source candidate.

G. FAKE-SOURCE INJECTION AT THE VELOCITY KINKS

We utilized `analysistools.extract.companions` to inject positive fake sources at specific positions with the goal of estimating the empirical detection limits at the locations of the ALMA velocity kinks #1 and #2. Figures 19 and 20 show the fake-source injection results at different contrast levels and KL modes. We adopted the empirical detection limits at the locations of the velocity kinks at the contrast levels at which we could spatially resolve the injected source from residual speckles and the disk features with $\text{KL} = 5$.

Due to the relatively small field rotation, aggressive strategies for PSF subtraction with $\text{KL} \geq 10$ induce more residuals of stellar light and speckles at $\rho \lesssim 2''$, while the injected fake source at kink #1 is well retrieved at smaller KL modes (see Figure 19). For the fake-source injection at kink #2, the location is so close to R1 that the PSF has an overlap with it. However, the derived empirical detection limit is better than the numerical contrast limit, which in turn is affected by the presence of R1 (see Section 4.2).

REFERENCES

Alarcón, F., Bergin, E. A., & Cugno, G. 2024, ApJ, 966, 225,

doi: [10.3847/1538-4357/ad3938](https://doi.org/10.3847/1538-4357/ad3938)



Figure 19. F410M post-processed images with different KL modes after injecting a fake source with different contrast levels ($\Delta F410M = 14.6\text{--}15.6$ mag) at the location of the ALMA velocity kink #1. The injected source is indicated by a white arrow in each image.

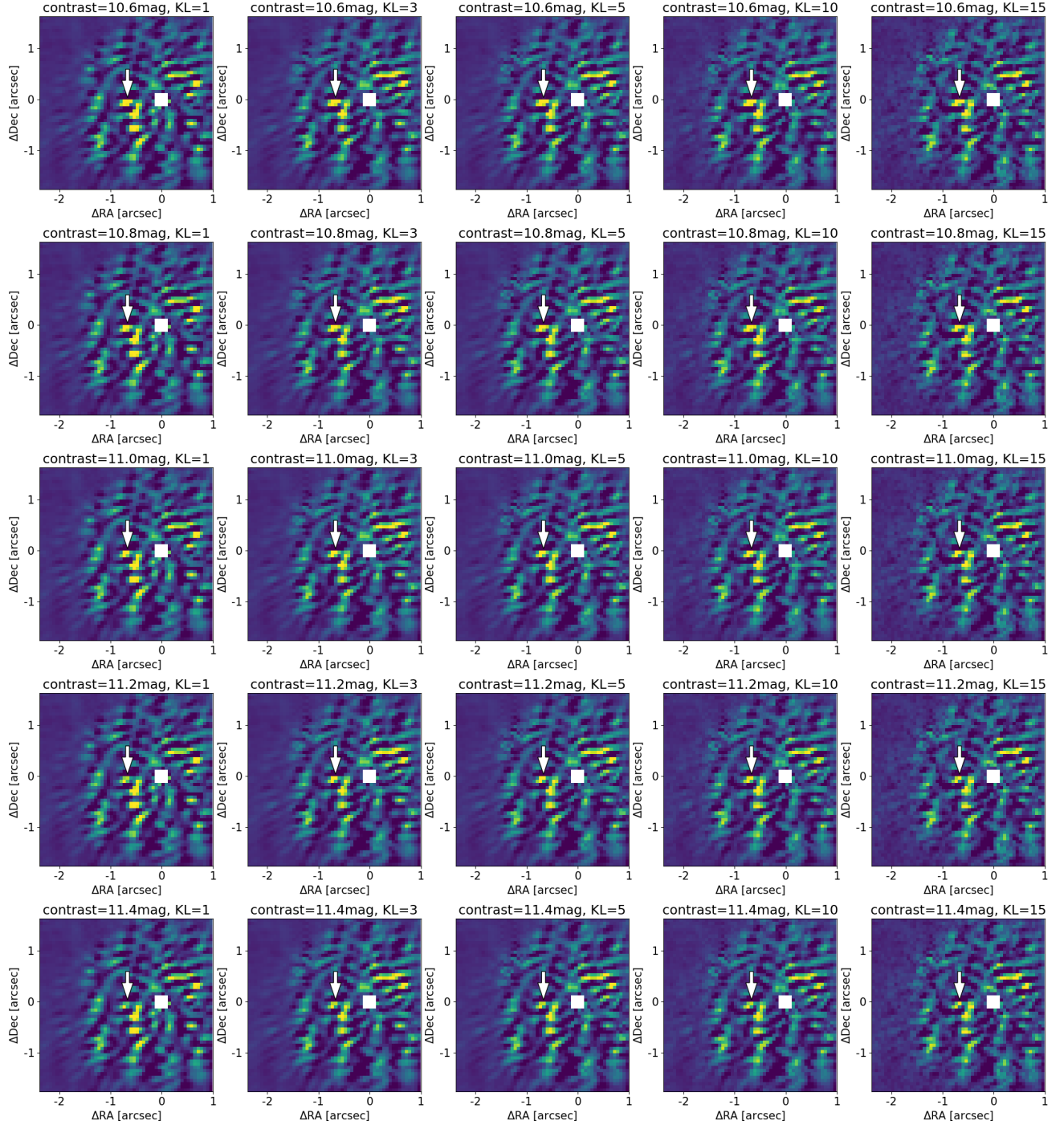


Figure 20. Same as in Figure 19 but with injected fake sources at the location of the ALMA velocity kink #2 (with contrast levels $\Delta F410M = 10.6\text{--}11.4$ mag).

- Andrews, S. M., Huang, J., Pérez, L. M., et al. 2018, *ApJL*, 869, L41, doi: [10.3847/2041-8213/aaf741](https://doi.org/10.3847/2041-8213/aaf741)
- Asensio-Torres, R., Henning, T., Cantalloube, F., et al. 2021, *A&A*, 652, A101, doi: [10.1051/0004-6361/202140325](https://doi.org/10.1051/0004-6361/202140325)
- Bae, J., Isella, A., Zhu, Z., et al. 2023, in *Astronomical Society of the Pacific Conference Series*, Vol. 534, *Protostars and Planets VII*, ed. S. Inutsuka, Y. Aikawa, T. Muto, K. Tomida, & M. Tamura, 423
- Banzatti, A., Pinilla, P., Ricci, L., et al. 2015, *ApJL*, 815, L15, doi: [10.1088/2041-8205/815/1/L15](https://doi.org/10.1088/2041-8205/815/1/L15)
- Baruteau, C., Crida, A., Paardekooper, S. J., et al. 2014, in *Protostars and Planets VI*, ed. H. Beuther, R. S. Klessen, C. P. Dullemond, & T. Henning, 667–689, doi: [10.2458/azu_uapress.9780816531240-ch029](https://doi.org/10.2458/azu_uapress.9780816531240-ch029)
- Bayo, A., Rodrigo, C., Barrado Y Navascués, D., et al. 2008, *A&A*, 492, 277, doi: [10.1051/0004-6361:200810395](https://doi.org/10.1051/0004-6361:200810395)
- Boehler, Y., Ricci, L., Weaver, E., et al. 2018, *ApJ*, 853, 162, doi: [10.3847/1538-4357/aaa19c](https://doi.org/10.3847/1538-4357/aaa19c)
- Brandl, B. R., Lenzen, R., Pantin, E., et al. 2010, in *Society of Photo-Optical Instrumentation Engineers (SPIE) Conference Series*, Vol. 7735, *Ground-based and Airborne Instrumentation for Astronomy III*, ed. I. S. McLean, S. K. Ramsay, & H. Takami, 77352G, doi: [10.1117/12.857346](https://doi.org/10.1117/12.857346)
- Burke, C. J., Christiansen, J. L., Mullally, F., et al. 2015, *ApJ*, 809, 8, doi: [10.1088/0004-637X/809/1/8](https://doi.org/10.1088/0004-637X/809/1/8)
- Burrows, A., Heng, K., & Nampaisarn, T. 2011, *ApJ*, 736, 47, doi: [10.1088/0004-637X/736/1/47](https://doi.org/10.1088/0004-637X/736/1/47)
- Bushouse, H., Eisenhamer, J., Dencheva, N., et al. 2023, *JWST Calibration Pipeline*, 1.11.2, Zenodo, doi: [10.5281/zenodo.8140011](https://doi.org/10.5281/zenodo.8140011)
- Carter, A. L., Hinkley, S., Kammerer, J., et al. 2023, *ApJL*, 951, L20, doi: [10.3847/2041-8213/acd93e](https://doi.org/10.3847/2041-8213/acd93e)
- Cugno, G., Quanz, S. P., Hunziker, S., et al. 2019, *A&A*, 622, A156, doi: [10.1051/0004-6361/201834170](https://doi.org/10.1051/0004-6361/201834170)
- Cugno, G., Pearce, T. D., Launhardt, R., et al. 2023, *A&A*, 669, A145, doi: [10.1051/0004-6361/202244891](https://doi.org/10.1051/0004-6361/202244891)
- Currie, T., Biller, B., Lagrange, A., et al. 2023, in *Astronomical Society of the Pacific Conference Series*, Vol. 534, *Protostars and Planets VII*, ed. S. Inutsuka, Y. Aikawa, T. Muto, K. Tomida, & M. Tamura, 799
- Currie, T., Lawson, K., Schneider, G., et al. 2022, *Nature Astronomy*, 6, 751, doi: [10.1038/s41550-022-01634-x](https://doi.org/10.1038/s41550-022-01634-x)
- de Gregorio-Monsalvo, I., Ménard, F., Dent, W., et al. 2013, *A&A*, 557, A133, doi: [10.1051/0004-6361/201321603](https://doi.org/10.1051/0004-6361/201321603)
- Dipierro, G., Ricci, L., Pérez, L., et al. 2018, *MNRAS*, 475, 5296, doi: [10.1093/mnras/sty181](https://doi.org/10.1093/mnras/sty181)
- Doi, K., & Kataoka, A. 2021, *ApJ*, 912, 164, doi: [10.3847/1538-4357/abe5a6](https://doi.org/10.3847/1538-4357/abe5a6)
- Dong, R., Liu, S.-y., Eisner, J., et al. 2018, *ApJ*, 860, 124, doi: [10.3847/1538-4357/aac6cb](https://doi.org/10.3847/1538-4357/aac6cb)
- Fitzgerald, M., Bailey, V., Baranec, C., et al. 2019, in *Bulletin of the American Astronomical Society*, Vol. 51, 251
- Flock, M., Ruge, J. P., Dzyurkevich, N., et al. 2015, *A&A*, 574, A68, doi: [10.1051/0004-6361/201424693](https://doi.org/10.1051/0004-6361/201424693)
- Gaia Collaboration, Prusti, T., de Bruijne, J. H. J., et al. 2016, *A&A*, 595, A1, doi: [10.1051/0004-6361/201629272](https://doi.org/10.1051/0004-6361/201629272)
- Gaia Collaboration, Vallenari, A., Brown, A. G. A., et al. 2023, *A&A*, 674, A1, doi: [10.1051/0004-6361/202243940](https://doi.org/10.1051/0004-6361/202243940)
- Ginski, C., Stolker, T., Pinilla, P., et al. 2016, *A&A*, 595, A112, doi: [10.1051/0004-6361/201629265](https://doi.org/10.1051/0004-6361/201629265)
- Goldreich, P., & Tremaine, S. 1979, *ApJ*, 233, 857, doi: [10.1086/157448](https://doi.org/10.1086/157448)
- Grady, C. A., Devine, D., Woodgate, B., et al. 2000, *ApJ*, 544, 895, doi: [10.1086/317222](https://doi.org/10.1086/317222)
- Greenbaum, A. Z., Llop-Sayson, J., Lew, B. W. P., et al. 2023, *ApJ*, 945, 126, doi: [10.3847/1538-4357/acb68b](https://doi.org/10.3847/1538-4357/acb68b)
- Guidi, G., Ruane, G., Williams, J. P., et al. 2018, *MNRAS*, 479, 1505, doi: [10.1093/mnras/sty1642](https://doi.org/10.1093/mnras/sty1642)
- Guidi, G., Isella, A., Testi, L., et al. 2022, *A&A*, 664, A137, doi: [10.1051/0004-6361/202142303](https://doi.org/10.1051/0004-6361/202142303)
- Haffert, S. Y., Bohn, A. J., de Boer, J., et al. 2019, *Nature Astronomy*, 3, 749, doi: [10.1038/s41550-019-0780-5](https://doi.org/10.1038/s41550-019-0780-5)
- Hammond, I., Christiaens, V., Price, D. J., et al. 2023, *MNRAS*, 522, L51, doi: [10.1093/mnras/lsad027](https://doi.org/10.1093/mnras/lsad027)
- Hasegawa, Y., Uyama, T., Hashimoto, J., et al. 2024, *AJ*, 167, 105, doi: [10.3847/1538-3881/ad1ccc](https://doi.org/10.3847/1538-3881/ad1ccc)
- Hinkley, S., Biller, B., Skemer, A., et al. 2023, *arXiv e-prints*, arXiv:2301.07199, doi: [10.48550/arXiv.2301.07199](https://doi.org/10.48550/arXiv.2301.07199)
- Hinz, P., Codona, J., Guyon, O., et al. 2012, in *Society of Photo-Optical Instrumentation Engineers (SPIE) Conference Series*, Vol. 8446, *Ground-based and Airborne Instrumentation for Astronomy IV*, ed. I. S. McLean, S. K. Ramsay, & H. Takami, 84461P, doi: [10.1117/12.926751](https://doi.org/10.1117/12.926751)
- Huang, J., Andrews, S. M., Dullemond, C. P., et al. 2018, *ApJL*, 869, L42, doi: [10.3847/2041-8213/aaf740](https://doi.org/10.3847/2041-8213/aaf740)
- Isella, A., Testi, L., Natta, A., et al. 2007, *A&A*, 469, 213, doi: [10.1051/0004-6361:20077385](https://doi.org/10.1051/0004-6361:20077385)
- Isella, A., Guidi, G., Testi, L., et al. 2016, *PhRvL*, 117, 251101, doi: [10.1103/PhysRevLett.117.251101](https://doi.org/10.1103/PhysRevLett.117.251101)
- Isella, A., Huang, J., Andrews, S. M., et al. 2018, *ApJL*, 869, L49, doi: [10.3847/2041-8213/aaf747](https://doi.org/10.3847/2041-8213/aaf747)
- Izquierdo, A. F., Facchini, S., Rosotti, G. P., van Dishoeck, E. F., & Testi, L. 2022, *ApJ*, 928, 2, doi: [10.3847/1538-4357/ac474d](https://doi.org/10.3847/1538-4357/ac474d)
- Izquierdo, A. F., Testi, L., Facchini, S., et al. 2023, *A&A*, 674, A113, doi: [10.1051/0004-6361/202245425](https://doi.org/10.1051/0004-6361/202245425)
- Juillard, S., Christiaens, V., Absil, O., Stasevic, S., & Milli, J. 2024, *A&A*, 688, A185, doi: [10.1051/0004-6361/202449747](https://doi.org/10.1051/0004-6361/202449747)

- Kammerer, J., Girard, J., Carter, A. L., et al. 2022, in Society of Photo-Optical Instrumentation Engineers (SPIE) Conference Series, Vol. 12180, Space Telescopes and Instrumentation 2022: Optical, Infrared, and Millimeter Wave, ed. L. E. Coyle, S. Matsuura, & M. D. Perrin, 121803N, doi: [10.1117/12.2628865](https://doi.org/10.1117/12.2628865)
- Kanagawa, K. D., Muto, T., Tanaka, H., et al. 2015, *ApJL*, 806, L15, doi: [10.1088/2041-8205/806/1/L15](https://doi.org/10.1088/2041-8205/806/1/L15)
- Keppler, M., Benisty, M., Müller, A., et al. 2018, *A&A*, 617, A44, doi: [10.1051/0004-6361/201832957](https://doi.org/10.1051/0004-6361/201832957)
- Lawson, K., Schlieder, J. E., Leisenring, J. M., et al. 2024, *ApJL*, 967, L8, doi: [10.3847/2041-8213/ad4496](https://doi.org/10.3847/2041-8213/ad4496)
- Leisenring, J. 2025, WebbPSF Extensions, v2.0.0, Zenodo, doi: [10.5281/zenodo.15033131](https://doi.org/10.5281/zenodo.15033131)
- Li, H., Li, S., Koller, J., et al. 2005, *ApJ*, 624, 1003, doi: [10.1086/429367](https://doi.org/10.1086/429367)
- Li, H., Lubow, S. H., Li, S., & Lin, D. N. C. 2009, *ApJL*, 690, L52, doi: [10.1088/0004-637X/690/1/L52](https://doi.org/10.1088/0004-637X/690/1/L52)
- Lin, D. N. C., Bodenheimer, P., & Richardson, D. C. 1996, *Nature*, 380, 606, doi: [10.1038/380606a0](https://doi.org/10.1038/380606a0)
- Lin, D. N. C., & Papaloizou, J. 1979, *MNRAS*, 186, 799, doi: [10.1093/mnras/186.4.799](https://doi.org/10.1093/mnras/186.4.799)
- Liu, S.-F., Jin, S., Li, S., Isella, A., & Li, H. 2018, *ApJ*, 857, 87, doi: [10.3847/1538-4357/aab718](https://doi.org/10.3847/1538-4357/aab718)
- Lodato, G., Dipierro, G., Ragusa, E., et al. 2019, *MNRAS*, 486, 453, doi: [10.1093/mnras/stz913](https://doi.org/10.1093/mnras/stz913)
- Marleau, G. D., Aoyama, Y., Kuiper, R., et al. 2022, *A&A*, 657, A38, doi: [10.1051/0004-6361/202037494](https://doi.org/10.1051/0004-6361/202037494)
- Mayor, M., & Queloz, D. 1995, *Nature*, 378, 355, doi: [10.1038/378355a0](https://doi.org/10.1038/378355a0)
- Mazoyer, J., Arriaga, P., Hom, J., et al. 2020, in Society of Photo-Optical Instrumentation Engineers (SPIE) Conference Series, Vol. 11447, Ground-based and Airborne Instrumentation for Astronomy VIII, ed. C. J. Evans, J. J. Bryant, & K. Motohara, 1144759, doi: [10.1117/12.2560091](https://doi.org/10.1117/12.2560091)
- Mendigutía, I., Brittain, S., Eiroa, C., et al. 2013, *ApJ*, 776, 44, doi: [10.1088/0004-637X/776/1/44](https://doi.org/10.1088/0004-637X/776/1/44)
- Mesa, D., Langlois, M., Garufi, A., et al. 2019, *MNRAS*, 488, 37, doi: [10.1093/mnras/stz1662](https://doi.org/10.1093/mnras/stz1662)
- Monnier, J. D., Kraus, S., Buscher, D., et al. 2014, in Society of Photo-Optical Instrumentation Engineers (SPIE) Conference Series, Vol. 9146, Optical and Infrared Interferometry IV, ed. J. K. Rajagopal, M. J. Creech-Eakman, & F. Malbet, 914610, doi: [10.1117/12.2057262](https://doi.org/10.1117/12.2057262)
- Muro-Arena, G. A., Dominik, C., Waters, L. B. F. M., et al. 2018, *A&A*, 614, A24, doi: [10.1051/0004-6361/201732299](https://doi.org/10.1051/0004-6361/201732299)
- Öberg, K. I., Guzmán, V. V., Walsh, C., et al. 2021, *ApJS*, 257, 1, doi: [10.3847/1538-4365/ac1432](https://doi.org/10.3847/1538-4365/ac1432)
- Owen, J. E., Ercolano, B., Clarke, C. J., & Alexander, R. D. 2010, *MNRAS*, 401, 1415, doi: [10.1111/j.1365-2966.2009.15771.x](https://doi.org/10.1111/j.1365-2966.2009.15771.x)
- Paardekooper, S., Dong, R., Duffell, P., et al. 2023, in Astronomical Society of the Pacific Conference Series, Vol. 534, Protostars and Planets VII, ed. S. Inutsuka, Y. Aikawa, T. Muto, K. Tomida, & M. Tamura, 685, doi: [10.48550/arXiv.2203.09595](https://doi.org/10.48550/arXiv.2203.09595)
- Packham, C., Honda, M., Richter, M., et al. 2012, in Society of Photo-Optical Instrumentation Engineers (SPIE) Conference Series, Vol. 8446, Ground-based and Airborne Instrumentation for Astronomy IV, ed. I. S. McLean, S. K. Ramsay, & H. Takami, 84467G, doi: [10.1117/12.924996](https://doi.org/10.1117/12.924996)
- Perrin, M. D., Sivaramakrishnan, A., Lajoie, C.-P., et al. 2014, in Society of Photo-Optical Instrumentation Engineers (SPIE) Conference Series, Vol. 9143, Space Telescopes and Instrumentation 2014: Optical, Infrared, and Millimeter Wave, ed. J. Oschmann, Jacobus M., M. Clampin, G. G. Fazio, & H. A. MacEwen, 91433X, doi: [10.1117/12.2056689](https://doi.org/10.1117/12.2056689)
- Pinte, C., Price, D. J., Ménard, F., et al. 2018, *ApJL*, 860, L13, doi: [10.3847/2041-8213/aac6dc](https://doi.org/10.3847/2041-8213/aac6dc)
- , 2020, *ApJL*, 890, L9, doi: [10.3847/2041-8213/ab6dda](https://doi.org/10.3847/2041-8213/ab6dda)
- Quanz, S. P., Ottiger, M., Fontanet, E., et al. 2022, *A&A*, 664, A21, doi: [10.1051/0004-6361/202140366](https://doi.org/10.1051/0004-6361/202140366)
- Ren, B. B., Wallack, N. L., Hurt, S. A., et al. 2023, *A&A*, 670, A162, doi: [10.1051/0004-6361/202244485](https://doi.org/10.1051/0004-6361/202244485)
- Ricci, L., Liu, S.-F., Isella, A., & Li, H. 2018, *ApJ*, 853, 110, doi: [10.3847/1538-4357/aaa546](https://doi.org/10.3847/1538-4357/aaa546)
- Rich, E. A., Wisniewski, J. P., Sitko, M. L., et al. 2020, *ApJ*, 902, 4, doi: [10.3847/1538-4357/abb2a3](https://doi.org/10.3847/1538-4357/abb2a3)
- Rich, E. A., Wisniewski, J. P., Currie, T., et al. 2019, *ApJ*, 875, 38, doi: [10.3847/1538-4357/ab0f3b](https://doi.org/10.3847/1538-4357/ab0f3b)
- Rieke, M. J., Kelly, D., & Horner, S. 2005, in Society of Photo-Optical Instrumentation Engineers (SPIE) Conference Series, Vol. 5904, Cryogenic Optical Systems and Instruments XI, ed. J. B. Heaney & L. G. Burrieschi, 1–8, doi: [10.1117/12.615554](https://doi.org/10.1117/12.615554)
- Sanchis, E., Picogna, G., Ercolano, B., Testi, L., & Rosotti, G. 2020, *MNRAS*, 492, 3440, doi: [10.1093/mnras/staa074](https://doi.org/10.1093/mnras/staa074)
- Serabyn, E., Huby, E., Matthews, K., et al. 2017, *AJ*, 153, 43, doi: [10.3847/1538-3881/153/1/43](https://doi.org/10.3847/1538-3881/153/1/43)
- Soummer, R., Pueyo, L., & Larkin, J. 2012, *ApJL*, 755, L28, doi: [10.1088/2041-8205/755/2/L28](https://doi.org/10.1088/2041-8205/755/2/L28)
- Spiegel, D. S., & Burrows, A. 2012, *ApJ*, 745, 174, doi: [10.1088/0004-637X/745/2/174](https://doi.org/10.1088/0004-637X/745/2/174)
- Suriano, S. S., Li, Z.-Y., Krasnopolsky, R., & Shang, H. 2018, *MNRAS*, 477, 1239, doi: [10.1093/mnras/sty1717](https://doi.org/10.1093/mnras/sty1717)
- Teague, R., Bae, J., & Bergin, E. A. 2019, *Nature*, 574, 378, doi: [10.1038/s41586-019-1642-0](https://doi.org/10.1038/s41586-019-1642-0)
- Teague, R., Bae, J., Bergin, E. A., Birnstiel, T., & Foreman-Mackey, D. 2018, *ApJL*, 860, L12, doi: [10.3847/2041-8213/aac6d7](https://doi.org/10.3847/2041-8213/aac6d7)
- Uribe, A. L., Klahr, H., Flock, M., & Henning, T. 2011, *ApJ*, 736, 85, doi: [10.1088/0004-637X/736/2/85](https://doi.org/10.1088/0004-637X/736/2/85)

- Uyama, T., Hashimoto, J., Kuzuhara, M., et al. 2017, *AJ*, 153, 106, doi: [10.3847/1538-3881/153/3/106](https://doi.org/10.3847/1538-3881/153/3/106)
- Wagner, K., Stone, J., Skemer, A., et al. 2023, *Nature Astronomy*, 7, 1208, doi: [10.1038/s41550-023-02028-3](https://doi.org/10.1038/s41550-023-02028-3)
- Wallack, N. L., Ruffio, J.-B., Ruane, G., et al. 2024, *AJ*, 168, 78, doi: [10.3847/1538-3881/ad390c](https://doi.org/10.3847/1538-3881/ad390c)
- Wang, J. J., Ruffio, J.-B., De Rosa, R. J., et al. 2015, in *Astrophysics Source Code Library*, ascl:1506.001. <http://ascl.net/1506.001>
- Wisniewski, J. P., Clampin, M., Grady, C. A., et al. 2008, *ApJ*, 682, 548, doi: [10.1086/589629](https://doi.org/10.1086/589629)
- Xie, C., Haffert, S. Y., de Boer, J., et al. 2020, *A&A*, 644, A149, doi: [10.1051/0004-6361/202038242](https://doi.org/10.1051/0004-6361/202038242)
- Zhang, S., Zhu, Z., Huang, J., et al. 2018, *ApJL*, 869, L47, doi: [10.3847/2041-8213/aaf744](https://doi.org/10.3847/2041-8213/aaf744)
- Zhu, Z. 2015, *ApJ*, 799, 16, doi: [10.1088/0004-637X/799/1/16](https://doi.org/10.1088/0004-637X/799/1/16)
- Zhu, Z., Andrews, S. M., & Isella, A. 2018, in *Astronomical Society of the Pacific Conference Series*, Vol. 517, *Science with a Next Generation Very Large Array*, ed. E. Murphy, 193